MOX-Report No. 21/2018

Comparing Isogeometric Analysis and Spectral Element Methods: accuracy and spectral properties

Gervasio, P.; Dede', L.; Chanon, O.; Quarteroni, A.

MOX, Dipartimento di Matematica
Politecnico di Milano, Via Bonardi 9 - 20133 Milano (Italy)

mox-dmat@polimi.it http://mox.polimi.it

Comparing Isogeometric Analysis and Spectral Element Methods: accuracy and spectral properties

Paola Gervasio[a], Luca Dedè[b,*], Ondine Chanon[c], Alfio Quarteroni[b,d]

[a] *DICATAM, Università degli Studi di Brescia, via Branze 38, I-25123 Brescia, Italy*
[b] *MOX, Department of Mathematics, Politecnico di Milano, Piazza Leonardo da Vinci 32, 20133 Milano, Italy*
[c] *MNS, Institute of Mathematics, École Polytechnique Fédérale de Lausanne, Station 8, CH-1015 Lausanne, Switzerland*
[d] *Institute of Mathematics, École Polytechnique Fédérale de Lausanne (EPFL), Station 8, CH-1015 Lausanne, Switzerland (Honorary professor)*

Abstract

In this paper, we carry out a systematic comparison between the theoretical properties of Spectral Element Methods (SEM) and NURBS–based Isogeometric Analysis (IGA) in the framework of the Galerkin method for the approximation of the Poisson problem. Our focus is on their convergence properties, the algebraic structure and the spectral properties of the corresponding discrete arrays (mass and stiffness matrices). We review the available theoretical results for these methods and verify them numerically by performing error analysis on the solution of the Poisson problem. Where theory is lacking, we use numerical investigation of the results to draw conjectures on the behavior of the corresponding theoretical laws in terms of the design parameters, such as the (mesh) element size, the local polynomial degree, the smoothness of the NURBS basis functions, the space dimension, and the total number of degrees of freedom involved in the computations.

Keywords: isogeometric analysis, *hp* finite element methods, spectral element methods, rate of convergence, condition number

1. Introduction

Spectral element methods (SEM) (see, e.g., [7]) and Isogeometric Analysis (IGA) (see, e.g., [8]) can be interpreted as two different paradigms for high order approximation of partial differential equations (PDEs); as a matter of fact, albeit IGA was not originally introduced with this aim, employing specific basis functions allows to interpret it as an high order method. Apart from their different use of basis functions, piecewise polynomials for SEM, B–spline or NURBS for IGA (with variable degree of continuity across element boundaries), the two approaches share many similarities. The perhaps more remarkable are reported below:

1 – they can be both recast in the framework of the Galerkin method: SEM is however most often used with inexact calculation of integrals using the so-called Gauss-Legendre-Lobatto numerical integration. This results into the so-called SEM-NI method (NI standing for numerical integration), which is the one we address in this paper. On the other side, for IGA, we consider the so called NURBS-based IGA in the framework of the Galerin method.;

*Corresponding author. E-mail: luca.dede@polimi.it

2 – the induced approximation error decays more than algebraically fast with respect to the local polynomial degree.

On the other hand, the two methods differ in what concerns the algebraic structures of the corresponding arrays (say, the mass and the stiffness matrices), the spectral properties of the latter (the behavior of their extreme eigenvalues, and the corresponding condition number), and the actual decay rate of the approximation error with respect to the discretization parameters: the element-size h, and the local polynomial degree p.

Our aim in this note is to report the most relevant theoretical results addressing the aforementioned issues. Most of the results on the rate of convergence of the approximation error are taken from the existing literature (see, e.g. [3, 4, 6, 7, 2, 10, 11]) and reorganize some of them for a better exploitation in our comparison. However, few of them are new. When the theory is missing we investigate these properties numerically and we propose the law of behavior in terms of h, p, the spatial dimension d, and the total number of degrees of freedom (dof).

Our analysis is concerned with the approximation of the mass matrix and the stiffness matrix for the Poisson boundary value problem in a cubic domain. We systematically compare SEM-NI with two realizations of IGA: IGA-C^0 (only the continuity across interelement boundaries is imposed on the problem solution, i.e. the NURBS basis functions are only globally C^0-continuous in the computational domain) and IGA-C^{p-1} (the continuity holds for the solution as well as for all its derivatives of order up to $p-1$, i.e. the NURBS basis functions are globally C^{p-1}-continuous in the computational domain).

In general terms we can concude that, errorwise, IGA-C^0 and SEM-NI behave essentially in the same way. For instance, their rate of convergence with respect to h scales (optimally) as p in the H^1-norm, and $(p+1)$ in the L^2- norm. IGA-C^{p-1} exhibits the same type of convergence, even if the errors it produces are larger than those provided by IGA-C^0 and SEM-NI with the same values of h and p, basically due to the (much) lower number of dofs involved in the discretization for the same value of h. When h is kept fixed and p is increased, IGA-C^0 and SEM-NI converge with a rate that is only dictated by the Sobolev regularity of the solution (hence exponentially fast in case the latter is analytical). The same is true for IGA-C^{p-1}, although with a slower rate of decay. IGA-C^{p-1} provides however the lowest error when the three methods are run with the same number of degrees of freedom.

On a different side, SEM-NI arrays are in general less dense and better conditioned than those of IGA-C^{p-1}. In particular, SEM-NI minimizes the error with respect to the number of non-zero entries of the stiffness matrix (those that undermine the computational cost of the stiffness matrix assembling and of the matrix-vector products for residual evaluations in iterative methods).

In the second part of the paper, the spectral analysis concerning the behavior of the extreme eigenvalues (and associated condition number) of IGA arrays (mass and stiffness matrices) complements the rather scarce literature available on the subject. More precisely starting from the numerical computation of the extreme eigenvalues for any spatial dimension $d = 1,\ 2,\ 3$, we mimic (with analytic laws) the real behavior of the spectral condition number of the IGA matrices against the local polynomial degree p and the element-size h.

While it is well known (see, e.g., [3, 23, 6, 7]) that the condition number of the SEM-NI stiffness matrix grows algebraically as $h^{-2}p^3$ for all h and p, the analysis of the present paper highlights that the spectral condition number of the IGA-C^0 stiffness matrix grows algebraically like $h^{-2}p^2$ when h is sufficently small w.r.t. p and exponentially like $p^{-d/2}4^{dp}$ otherwise; moreover, the spectral condition number of the IGA-C^{p-1} stiffness matrix grows algebraically like $h^{-2}p$ when h

is sufficently small w.r.t. p and exponentially, at least like pe^{dp}, otherwise.

The condition number of the SEM-NI mass matrix grows algebraically like p^d, while we find that the condition numbers of the IGA mass matrices (either IGA-C^0 and IGA-C^{p-1}) grow exponentially with p.

A specific outline of the paper is as follows.

In Section 2 we present the Poisson problem, its discretization by SEM-NI (in particular we describe how to deal with curved boundaries in the SEM context for $d = 2$ and $d = 3$ by exploiting transfinite mappings) and by IGA methods, then we resume the theoretical convergence estimates for both the approaches. In Section 3 we compare the numerical convergence rates of the methods when they are applied to solve the Poisson problem with given solution. In the first test case we solve the differential problem on the cube domain with either SEM-NI, IGA-C^0 and IGA-C^{p-1}. In the second one we consider a more general domain with curved boundary and compare the convergence curves of SEM-NI and IGA-C^{p-1} approximations, as well as the CPUtimes needed to assemble the stiffness matrices. Finally Section 4 is devoted to the spectral analysis of both the stiffness and mass matrices. After reviewing theoretical results known in literature, we present our conjectures (based on the numerical computations of extreme eigenvalues) about the behavior of the spectral condition number of IGA matrices versus both p and h.

This review addresses for the first time a systematic comparison of the theoretical properties of two classes of methods that are very popular and highly appreciated in the community of numerical analysts and computational scientists. We are confident that this analysis will be useful for a comparative assessment of the two approaches and a better awarefulness of their strengths and limitations.

2. Problem setting

Let $\Omega \subset \mathbb{R}^d$, with $d = 1, 2, 3$, be a bounded domain (when $d \geq 2$ we require that the boundary $\partial\Omega$ is Lipschitz continuous), and let $f \in L^2(\Omega)$ and $g \in H^{1/2}(\partial\Omega)$ be two given functions. Our reference Poisson problem, which we use through most of the paper as a benchmark problem, reads

$$\begin{cases} -\Delta u = f & \text{in } \Omega \\ u = g & \text{on } \partial\Omega. \end{cases} \tag{1}$$

We denote by $\widetilde{g}$ a lifting of the Dirichlet datum g, i.e. any function $\widetilde{g} \in H^1(\Omega)$ such that $\widetilde{g}|_{\partial\Omega} = g$. The weak form of problem (1) reads: find $u = (u^0 + \widetilde{g}) \in H^1(\Omega)$ with $u^0 \in V = H^1_0(\Omega)$ such that

$$a(u^0, v) = \mathcal{F}(v) - a(\widetilde{g}, v) \qquad \forall v \in V, \tag{2}$$

where $a(u, v) = \displaystyle\int_\Omega \nabla u \cdot \nabla v \; d\Omega$ and $\mathcal{F}(v) = \displaystyle\int_\Omega fv \; d\Omega$. Problem (2) admits a unique solution (see, e.g., [24]) that is stable w.r.t. the data f and g.

2.1. Discretization by the Spectral Element Method (SEM)

Given $h > 0$, let $\mathcal{T}_h$ be a family of partitions of the computational domain $\Omega \subset \mathbb{R}^d$ in ne_h quads (intervals when $d = 1$, quadrilaterals when $d = 2$, and hexaedra when $d = 3$). Following standard assumptions we require $\mathcal{T}_h$ to be conformal, regular, and quasi-uniform (see [24, Ch. 3]). We denote by $\hat{T}$ the reference element, i.e. the $d-$dimensional cube $(-1, 1)^d$ and let each element $T_\ell \in \mathcal{T}_h$ be the image of the reference element $\hat{T}$ through a sufficiently smooth one-to-one map

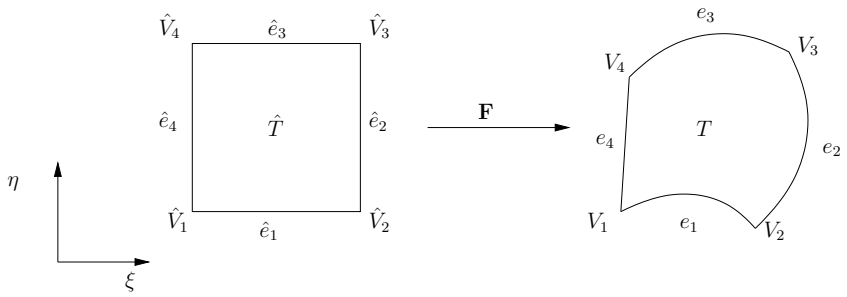

Figure 1: SEM mapping of the reference element $\hat{T} = [-1, 1]^2$ into a curved quadrilateral T

$\mathbf{F}_\ell : \hat{T} \to T_\ell$ with a sufficiently smooth inverse $\mathbf{F}_\ell^{-1} : T_\ell \to \hat{T}$. If $\mathbf{F}_\ell$ is affine, then the element T_ℓ is a parallelogram (when $d = 2$) or a parallelepipedon (when $d = 3$).

To deal with more general domains, also in the case of curved boundaries, we consider transfinite mappings introduced in [17, 18, 19]. Among the many possible choices proposed in the cited references, we choose the maps that guarantee $\mathbf{F}_\ell(\partial\hat{T}) = \partial T_\ell$ for any $T_\ell \in \mathcal{T}_h$. They are defined as follows.

Let us begin with $d = 2$ and let $\hat{T} = [-1, 1]^2$ be the reference element whose vertices $\hat{V}_1, \ldots, \hat{V}_4$ and edges $\hat{e}_1, \ldots, \hat{e}_4$ are ordered as in Fig. 1, while T (for simplicity we omit the index ℓ) denotes the generic element of $\mathcal{T}_h$ with vertices $V_1, \ldots, V_4$ and (possibly curved) edges $e_1, \ldots, e_4$.

The transfinite mapping $\mathbf{F} : \hat{T} \to T$ is expressed in terms of the parametrizations $\boldsymbol{\pi}_i : [-1, 1] \to e_i$ (for $i = 1, \ldots, 4$) of the edges (for any $\xi \in [-1, 1]$, $\boldsymbol{\pi}_i(\xi) \in \mathbb{R}^2$). Given $\boldsymbol{\pi}_1, \ldots, \boldsymbol{\pi}_4$ such that

$$\begin{aligned} V_1 &= \boldsymbol{\pi}_1(-1) = \boldsymbol{\pi}_4(-1), \qquad & V_2 &= \boldsymbol{\pi}_1(+1) = \boldsymbol{\pi}_2(-1), \\ V_3 &= \boldsymbol{\pi}_2(+1) = \boldsymbol{\pi}_3(+1), \qquad & V_4 &= \boldsymbol{\pi}_4(+1) = \boldsymbol{\pi}_3(-1), \end{aligned} \tag{3}$$

any $(\xi, \eta) \in \hat{T}$ is mapped into the corresponding point $(x, y) \in T$ by

$$\begin{aligned} (x, y) = \mathbf{F}(\xi, \eta) = \; & \frac{1-\eta}{2}\boldsymbol{\pi}_1(\xi) + \frac{1+\eta}{2}\boldsymbol{\pi}_3(\xi) \\ & + \frac{1-\xi}{2}\Big[\boldsymbol{\pi}_4(\eta) - \frac{1-\eta}{2}\boldsymbol{\pi}_4(-1) - \frac{1+\eta}{2}\boldsymbol{\pi}_4(1)\Big] \\ & + \frac{1+\xi}{2}\Big[\boldsymbol{\pi}_2(\eta) - \frac{1-\eta}{2}\boldsymbol{\pi}_2(-1) - \frac{1+\eta}{2}\boldsymbol{\pi}_2(1)\Big]. \end{aligned} \tag{4}$$

It is easy to verify that $\mathbf{F}(\hat{V}_i) = V_i$ and $\mathbf{F}(\hat{e}_i) = e_i$ for $i = 1, \ldots, 4$.

When $d = 3$, let $\hat{T} = (-1, 1)^3$ be the reference cube and (ξ, η, ζ) any point in $\hat{T}$. The faces $\hat{f}_1, \ldots, \hat{f}_6$ of $\hat{T}$ are ordered as follows: $\hat{f}_1$ belongs to the plane $\eta = -1$ and its vertices are $\hat{V}_1$, $\hat{V}_2$, $\hat{V}_6$, $\hat{V}_5$; $\hat{f}_2$ belongs to the plane $\xi = 1$ and its vertices are $\hat{V}_2$, $\hat{V}_3$, $\hat{V}_7$, $\hat{V}_6$; $\hat{f}_3$ belongs to the plane $\eta = 1$ and its vertices are $\hat{V}_4$, $\hat{V}_3$, $\hat{V}_7$, $\hat{V}_8$; $\hat{f}_4$ belongs to the plane $\xi = -1$ and its vertices are $\hat{V}_1$, $\hat{V}_4$, $\hat{V}_8$, $\hat{V}_5$; $\hat{f}_5$ belongs to the plane $\zeta = -1$ and its vertices are $\hat{V}_1$, $\hat{V}_2$, $\hat{V}_3$, $\hat{V}_4$; $\hat{f}_6$ belongs to the plane $\zeta = 1$ and its vertices are $\hat{V}_5$, $\hat{V}_6$, $\hat{V}_7$, $\hat{V}_8$ (see Fig. 2). The edges $\hat{e}_1, \ldots, \hat{e}_{12}$ are counterclockwise ordered, first those on the bottom horizontal plane, then those on the top horizontal plane and finally the vertical ones, thus, for example, the end-points of $\hat{e}_1$ are $\hat{V}_1$ and $\hat{V}_2$, the end-points of $\hat{e}_5$ are $\hat{V}_5$ and $\hat{V}_6$, and the end-points of $\hat{e}_9$ are $\hat{V}_1$ and $\hat{V}_5$.

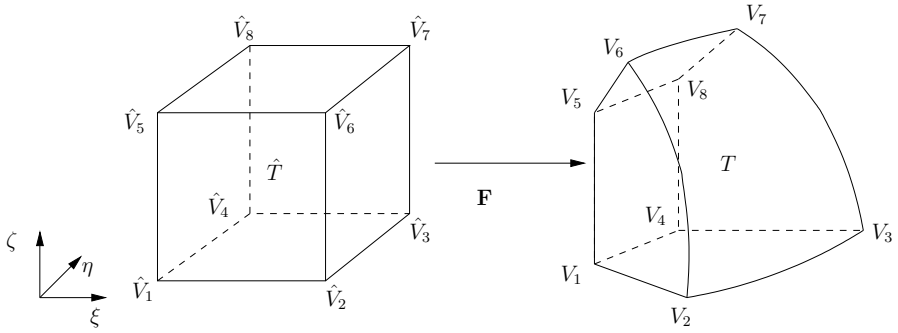

Figure 2: SEM mapping of the reference element $\hat{T} = [-1,1]^3$ into a curved hexahedron T

Let T denote the generic element of $\mathcal{T}_h$ with possibly curved faces $f_1, \ldots, f_6$. The transfinite mapping $\mathbf{F} : \hat{T} \to T$ is expressed in terms of the parametrizations $\mathbf{\Pi}_\ell : [-1,1]^2 \to f_\ell$ (for $\ell = 1, \ldots, 6$) of the faces of T (for any $(\xi, \eta) \in [-1,1]^2$, $\mathbf{\Pi}_\ell(\xi, \eta) \in \mathbb{R}^3$). Given $\mathbf{\Pi}_1,\ \mathbf{\Pi}_3 : (\xi, \zeta) \to \mathbb{R}^3$, $\mathbf{\Pi}_2,\ \mathbf{\Pi}_4 : (\eta, \zeta) \to \mathbb{R}^3$ and $\mathbf{\Pi}_5,\ \mathbf{\Pi}_6 : (\xi, \eta) \to \mathbb{R}^3$ such that

$$
\begin{aligned}
&e_1 = \mathbf{\Pi}_1(\cdot,-1) = \mathbf{\Pi}_5(\cdot,-1), && e_2 = \mathbf{\Pi}_2(\cdot,-1) = \mathbf{\Pi}_5(+1,\cdot),\\
&e_3 = \mathbf{\Pi}_3(\cdot,-1) = \mathbf{\Pi}_5(\cdot,+1), && e_4 = \mathbf{\Pi}_4(\cdot,-1) = \mathbf{\Pi}_5(-1,\cdot),\\
&e_5 = \mathbf{\Pi}_1(\cdot,+1) = \mathbf{\Pi}_6(\cdot,-1), && e_6 = \mathbf{\Pi}_2(\cdot,+1) = \mathbf{\Pi}_6(+1,\cdot),\\
&e_7 = \mathbf{\Pi}_3(\cdot,+1) = \mathbf{\Pi}_6(\cdot,+1), && e_8 = \mathbf{\Pi}_4(\cdot,+1) = \mathbf{\Pi}_6(-1,\cdot),\\
&e_9 = \mathbf{\Pi}_1(-1,\cdot) = \mathbf{\Pi}_4(-1,\cdot), && e_{10} = \mathbf{\Pi}_1(+1,\cdot) = \mathbf{\Pi}_2(-1,\cdot),\\
&e_{11} = \mathbf{\Pi}_2(+1,\cdot) = \mathbf{\Pi}_3(+1,\cdot), && e_{12} = \mathbf{\Pi}_3(-1,\cdot) = \mathbf{\Pi}_4(+1,\cdot),
\end{aligned}
\tag{5}
$$

any $(\xi, \eta, \zeta) \in \hat{T}$ is mapped into the corresponding point $(x, y, z) \in T$ by

$$
\begin{aligned}
(x,y,z) = \mathbf{F}(\xi,\eta,\zeta) = \ & \frac{1-\eta}{2}\mathbf{\Pi}_1(\xi,\zeta) + \frac{1+\eta}{2}\mathbf{\Pi}_3(\xi,\zeta)\\
&+\frac{1-\xi}{2}\Big[\mathbf{\Pi}_4(\eta,\zeta) - \frac{1-\eta}{2}\mathbf{\Pi}_4(-1,\zeta) - \frac{1+\eta}{2}\mathbf{\Pi}_4(1,\zeta)\Big]\\
&+\frac{1+\xi}{2}\Big[\mathbf{\Pi}_2(\eta,\zeta) - \frac{1-\eta}{2}\mathbf{\Pi}_2(-1,\zeta) - \frac{1+\eta}{2}\mathbf{\Pi}_2(1,\zeta)\Big]\\
&+\frac{1-\zeta}{2}\Big[\mathbf{\Pi}_5(\xi,\eta) - \frac{1-\xi}{2}\mathbf{\Pi}_5(-1,\eta) - \frac{1+\xi}{2}\mathbf{\Pi}_5(1,\eta)\\
&\quad -\frac{1-\eta}{2}\Big(\mathbf{\Pi}_5(\xi,-1) - \frac{1-\xi}{2}\mathbf{\Pi}_5(-1,-1) - \frac{1+\xi}{2}\mathbf{\Pi}_5(1,-1)\Big)\\
&\quad -\frac{1+\eta}{2}\Big(\mathbf{\Pi}_5(\xi,1) - \frac{1-\xi}{2}\mathbf{\Pi}_5(-1,1) - \frac{1+\xi}{2}\mathbf{\Pi}_5(1,1)\Big)\Big]\\
&+\frac{1+\zeta}{2}\Big[\mathbf{\Pi}_6(\xi,\eta) - \frac{1-\xi}{2}\mathbf{\Pi}_6(-1,\eta) - \frac{1+\xi}{2}\mathbf{\Pi}_6(1,\eta)\\
&\quad -\frac{1-\eta}{2}\Big(\mathbf{\Pi}_6(\xi,-1) - \frac{1-\xi}{2}\mathbf{\Pi}_6(-1,-1) - \frac{1+\xi}{2}\mathbf{\Pi}_6(1,-1)\Big)\\
&\quad -\frac{1+\eta}{2}\Big(\mathbf{\Pi}_6(\xi,1) - \frac{1-\xi}{2}\mathbf{\Pi}_6(-1,1) - \frac{1+\xi}{2}\mathbf{\Pi}_6(1,1)\Big)\Big].
\end{aligned}
\tag{6}
$$

Then, $\mathbf{F}(\hat{f}_\ell) = f_\ell$ for $\ell = 1, \ldots, 6$, $\mathbf{F}(\hat{e}_i) = e_i$ for $i = 1, \ldots, 12$ and $\mathbf{F}(\hat{V}_j) = V_j$ for $j = 1, \ldots, 8$. Notice that, when the map $\mathbf{\Pi}_\ell$ defining the face f_ℓ is not known explicitly, then it can be obtained from (4) in terms of the maps $\boldsymbol{\pi}_{\ell_1}, \ldots, \boldsymbol{\pi}_{\ell_4}$ associated with the four edges of f_ℓ.

So far, each element can be viewed as the image of a transfinite map $\mathbf{F}_k$ defined in either (4) (if $d = 2$) or (6) (if $d = 3$); in order to guarantee the conformity of the mesh, if T_k and T_m share a common edge or a face, say Γ_{km}, then $\mathbf{F}_k$ and $\mathbf{F}_m$ must agree there, i.e. $\mathbf{F}_k|_{\Gamma_{km}} \equiv \mathbf{F}_m|_{\Gamma_{km}}$.

Formulation. Given an integer $p \geq 1$, let us denote by $\mathbb{Q}_p$ the space of polynomials of degree less than or equal to p with respect to each independent variable ξ, η, ζ. We introduce the following finite dimensional spaces in $\overline{\Omega}$:

$$X_\delta = \{v \in C^0(\overline{\Omega}) \,:\, v_{|T_k} \in \mathbb{Q}_p \circ \mathbf{F}_k^{-1},\ \forall T_k \in \mathcal{T}_h\}, \quad V_\delta = V \cap X_\delta = \{v \in X_\delta \,:\, v_{|\partial\Omega} = 0\}. \tag{7}$$

δ is an abridged notation undermining the mesh size h and the local polynomial degree p.

Let $\widetilde{g}_\delta \in X_\delta$ denote any discrete approximation of the lifting $\widetilde{g}$. The Galerkin approximation of (2) reads: find $u_\delta = (u_\delta^0 + \widetilde{g}_\delta) \in X_\delta$ with $u_\delta^0 \in V_\delta$ such that

$$a(u_\delta^0, v_\delta) = \mathcal{F}(v_\delta) - a(\widetilde{g}_\delta, v_\delta) \qquad \forall v_\delta \in V_\delta. \tag{8}$$

Typically, when using SEM, the exact integrals appearing in a and $\mathcal{F}$ are replaced by the composite Legendre-Gauss-Lobatto (LGL) quadrature formulas (see [6]) with the aim of reducing the computational effort. This is exactly the approach that we consider in this paper, i.e the so called SEM with Numerical Integration (SEM-NI) at the LGL nodes [7].

For any integer $p \geq 1$, the $(p+1)$ LGL nodes and weights are first defined on the reference interval $[-1, 1]$ (see [6, formula (2.3.12)]) and then tensorized and mapped into the generic quad $T_\ell \in \mathcal{T}_h$ by applying the transfinite map $\mathbf{F}_\ell$. Let $\mathbf{x}_{\ell,q}$ and $w_{\ell,q}$, with $q = 1, \ldots, (p+1)^d$, denote the quadrature nodes and weights on T_ℓ for any $T_\ell \in \mathcal{T}_h$ and let ne_h be the number of elements in $\mathcal{T}_h$. By setting

$$a_\delta(u_\delta, v_\delta) = \sum_{\ell=1}^{ne_h} \sum_{q=1}^{(p+1)^d} \nabla u_\delta(\mathbf{x}_{\ell,q}) \cdot \nabla v_\delta(\mathbf{x}_{\ell,q}) w_{\ell,q}, \tag{9}$$

$$\mathcal{F}_\delta(v_\delta) = (f, v_\delta)_\delta = \sum_{\ell=1}^{ne_h} \sum_{q=1}^{(p+1)^d} f(\mathbf{x}_{\ell,q}) v_\delta(\mathbf{x}_{\ell,q}) w_{\ell,q}, \tag{10}$$

the discrete Galerkin formulation of (2) with Numerical Integration (SEM-NI) reads: find $u_\delta = (u_\delta^0 + \widetilde{g}_\delta) \in X_\delta$ with $u_\delta^0 \in V_\delta$ such that

$$a_\delta(u_\delta^0, v_\delta) = \mathcal{F}_\delta(v_\delta) - a_\delta(\widetilde{g}_\delta, v_\delta) \qquad \forall v_\delta \in V_\delta. \tag{11}$$

Algebraic form. Le us denote by $N = N(h, p)$ the total number of (non-repeated) LGL quadrature nodes $\mathbf{x}_i$ of $\mathcal{T}_h$. In order to represent the discrete solution u_δ, the nodal Lagrange basis functions $\varphi_i(\mathbf{x})$ (for $i = 1, \ldots, N$) defined over the set of LGL quadrature nodes $\{\mathbf{x}_i\}$ are used, thus we have

$$u_\delta(\mathbf{x}) = \sum_{i=1}^{N} u_i \varphi_i(\mathbf{x}), \tag{12}$$

where $u_i = u_\delta(\mathbf{x}_i)$. Typically $\widetilde{g}_\delta$ is chosen to be the Lagrange interpolant of g at the boundary nodes, extended to zero at all internal nodes of Ω, i.e.

$$\widetilde{g}_\delta(\mathbf{x}_i) = \begin{cases} g(\mathbf{x}_i) & \text{if } \mathbf{x}_i \in \mathcal{T}_h \cap \partial\Omega, \\ 0 & \text{if } \mathbf{x}_i \in \mathcal{T}_h \setminus \partial\Omega. \end{cases}$$

The SEM-NI stiffness matrix is defined by

$$(K_{SEM})_{ij} = a_\delta(\varphi_j, \varphi_i), \qquad i,j = 1,\dots,N, \tag{13}$$

while the SEM-NI mass matrix by

$$(M_{SEM})_{ij} = (\varphi_j, \varphi_i)_\delta, \qquad i,j = 1,\dots,N. \tag{14}$$

Thanks to the fact that the interpolation nodes coincide with the quadrature nodes, and noticing that the Lagrange basis functions are orthogonal with respect to the discrete inner product $(\cdot,\cdot)_\delta$, the SEM-NI mass matrix M_{SEM} is diagonal.

Let N^0 denote the number of degrees of freedom internal to Ω (we reorder all the mesh nodes so that the first N^0 are the internal ones), then we set $\mathbf{u}_{SEM} = [u_i]_{i=1}^{N^0}$, $\mathbf{f}_{SEM} = [f(\mathbf{x}_i)]_{i=1}^{N^0}$ and $\mathbf{g}_{SEM}$ s.t.

$$(\mathbf{g}_{SEM})_i = \sum_{j=N^0+1}^{N} (K_{SEM})_{ij} g(\mathbf{x}_j) \qquad \text{for } i = 1,\dots,N^0.$$

The algebraic form of (11) reads:

$$K_{SEM}\mathbf{u}_{SEM} = M_{SEM}\mathbf{f}_{SEM} - \mathbf{g}_{SEM}, \tag{15}$$

where we understand that both K_{SEM} and M_{SEM} are restricted to the rows $i = 1,\dots,N^0$ and the columns $j = 1,\dots,N^0$.

The equivalent system

$$(M_{SEM})^{-1}K_{SEM}\mathbf{u}_{SEM} = \mathbf{f}_{SEM} - (M_{SEM})^{-1}\mathbf{g}_{SEM} \tag{16}$$

represents instead the algebraic counterpart of the *collocation* approximation to problem (1) at the LGL quadrature nodes (see [6]).

Both M_{SEM} and K_{SEM} are symmetric positive definite (s.p.d.) matrices.
$(M_{SEM})^{-1}K_{SEM}$ is not symmetric any more, however it is similar to (and therefore share the same eigenvalues of) the s.p.d. matrix $(M_{SEM})^{-1/2}K_{SEM}(M_{SEM})^{-1/2}$.

Error estimates. The quadrature error produced by the LGL formulas decays with *spectral* accuracy, i.e., there exists $c = c(\Omega) > 0$ such that, for any $f \in H^s(\Omega)$, with $s \geq 1$, and for any $v_\delta \in V_\delta$ it holds (see [6, Sect. 5.4.3] and standard scaling arguments)

$$|(f, v_\delta) - (f, v_\delta)_\delta| \leq c(\Omega)\, p^{-s}\, h^s \|f\|_{H^s(\Omega)}\, \|v_\delta\|_{L^2(\Omega)}. \tag{17}$$

Let us assume for the sake of simplicity that $g = 0$ in (1). By using (17) and the Strang Lemma, the following approximation error can be proved: if $u \in H^s(\Omega)$ is the solution of (2) with $f \in H^q(\Omega)$ ($q \geq 0$) and u_δ is the solution of the SEM-NI problem (11) (notice that $u_\delta = u_\delta^0$) then (see [3, 6, 7])

$$\|u - u_\delta\|_{H^r(\Omega)} \leq c \left(h^{\min(s,p+1)-r}\, p^{r-s}\, \|u\|_{H^s(\Omega)} + h^{\min(q,p+1)}\, p^{-q}\, \|f\|_{H^q(\Omega)} \right) \tag{18}$$
$$0 \leq r \leq 1, \quad s > d/2,$$

where $c = c(s, q, \Omega)$ is independent of both h and p. A key ingredient to prove (18) is the following interpolation error estimate ([3, 6, 7])

$$\|u - \mathcal{I}_\delta u\|_{H^r(\Omega)} \leq c\, h^{\min(s,p+1)-r}\, p^{r-s}\, \|u\|_{H^s(\Omega)} \qquad 0 \leq r \leq 1, \quad s > d/2, \tag{19}$$

where $\mathcal{I}_\delta : C^0(\Omega) \to X_\delta$ is the Lagrange interpolation operator at the LGL nodes.

If f is integrated exactly by the LGL quadrature formulas, the convergence estimate (18) simplifies as follows

$$\|u - u_\delta\|_{H^r(\Omega)} \leq c\, h^{\min(s,p+1)-r}\, p^{r-s}\, \|u\|_{H^s(\Omega)} \quad 0 \leq r \leq 1, \quad s > r. \tag{20}$$

If, in particular, $s > p + 1$ and $r = 1$, (20) becomes

$$\|u - u_\delta\|_{H^1(\Omega)} \leq c \left(\frac{h}{p}\right)^p \frac{1}{p^{s-p-1}} \|u\|_{H^s(\Omega)}. \tag{21}$$

If the mesh is uniform and generated through the tensor-product rule, the total number ne_h of spectral elements can be written as $ne_h = (c/h)^d$, with c depending only on Ω, so that the total number of degrees of freedom reads $N = (p\, c/h + 1)^d \sim \left(\frac{p}{h}\right)^d$. Thus, (21) can be expressed in terms of N as follows

$$\|u - u_\delta\|_{H^1(\Omega)} \leq c\, N^{-p/d}\, \frac{1}{p^{s-p-1}}\, \|u\|_{H^s(\Omega)}. \tag{22}$$

2.2. Discretization by Isogeometric Analysis (IGA)

B-splines. Let $Z = \{0 = \zeta_0, \zeta_1, \ldots, \zeta_{n-1}, \zeta_n = 1\}$ be the set of $(n + 1)$ distinct knot values in the one-dimensional patch $[0, 1]$ and, given two positive integers p and k with $0 \leq k \leq p - 1$, let

$$\Xi^{(k)} = \{\xi_1, \xi_2, \ldots, \xi_q\} = \{\underbrace{\zeta_0, \ldots, \zeta_0}_{p+1}, \underbrace{\zeta_1, \ldots, \zeta_1}_{p-k}, \ldots, \underbrace{\zeta_{n-1}, \ldots, \zeta_{n-1}}_{p-k}, \underbrace{\zeta_n, \ldots, \zeta_n}_{p+1}\} \tag{23}$$

be the (ordered) $p-$open knot vector with a fixed number of repetitions. Notice that in this paper we specifically assume that all the internal knot values $\zeta_1, \ldots, \zeta_{n-1}$ are repeated $p - k$ times. This implies that the cardinality of $\Xi^{(k)}$ is $q = (p - k)(n - 1) + 2p + 2$. In an open knot-vector $\Xi^{(k)}$, as that under consideration in this paper, the two extreme knots (values) are repeated exactly $p + 1$ times. Then, after setting

$$B_{i,0}(\xi) = \begin{cases} 1 & \text{if } \xi_i \leq \xi < \xi_{i+1} \\ 0 & \text{otherwise,} \end{cases} \tag{24}$$

we define the univariate B-splines basis functions of local degree $p \geq 1$ and regularity C^k in [0,1] by means of the Cox-de Boor recursion formula as follows ([8]):

$$B_{i,p}(\xi) = \frac{\xi - \xi_i}{\xi_{i+p} - \xi_i} B_{i,p-1}(\xi) + \frac{\xi_{i+p+1} - \xi}{\xi_{i+p+1} - \xi_{i+1}} B_{i+1,p-1}(\xi). \tag{25}$$

The basis functions $B_{i,p}$ intrinsically depend on (and inherit all their properties from) the knots ξ_i. A most prominent property is the regularity. For that, we assume in this paper that all the basis functions are globally C^k-continuous in the patch (for a suitable k, with $0 \leq k \leq p - 1$, that stands for the global order of regularity), and in particular at all the internal knot values in Z.

In order to comply with the existing literature, we also understand the dependence of the basis functions on k.

When p, n, and k are fixed, the number of linearly independent B-splines $B_{i,p}$ is $n_b = (n-1)(p-k)+(p+1)$. We will consider the two extreme values for k. When $k=0$, the B-splines are only globally C^0 and we use the notation IGA-C^0 to identify this case. When $k=p-1$, the B-splines are globally C^{p-1} and we write IGA-C^{p-1} to identify this case.

The d-times tensor product of the set Z induces a cartesian grid in the parametric domain $\widehat{\Omega} = (0,1)^d$. If we assume for the sake of simplicity that the knots ζ_i are equally spaced along all the parametric directions, then the mesh size is $h = 1/n$. When the geometric dimension d of the computational domain is larger than 1, we exploit the tensor product rule for the set $\Xi^{(k)}$ and the B-splines functions. Then, for any $\boldsymbol{\xi} = (\xi^1, \dots, \xi^d) \in \widehat{\Omega}$, let

$$\psi_{i,p}(\boldsymbol{\xi}) = B_{i_1,p}(\xi^1) \cdots B_{i_d,p}(\xi^d) \tag{26}$$

be the generic multivariate B-spline basis function, with $i_k = 1, \dots, n_b$ for any $k = 1, \dots, d$ and with $i = 1, \dots, N_b = n_b^d$, with lexicographic ordering. Notice that $\xi^1 = \xi$ in the univariate case.

NURBS. Univariate NURBS basis functions are built starting from univariate B-splines by associating a set of *weights* $\{w_1, w_2, \dots, w_{n_b}\}$ with each of them; we assume in this paper that $w_i \in \mathbb{R}$ and $w_i > 0$ for all $i = 1, \dots, n_b$. The i-th univariate NURBS basis function reads:

$$N_{i,p}(\xi) = \frac{w_i \, B_{i,p}(\xi)}{\sum_{j=1}^{n_b} w_j \, B_{j,p}(\xi)}. \tag{27}$$

NURBS inherit properties from their B-splines counterpart, specifically the regularity property as the global C^k-continuity in the patch; we notice however that NURBS are not piecewise polynomials, for which p stands for the polynomial degree of the B-splines from which these are built. Multivariate NURBS basis functions are built by exploiting the d-times tensor product structure, thus yielding basis functions $\psi_{i,p}(\boldsymbol{\xi})$ in the form of equation (26). Unless than otherwise specified, we consider in this paper $\psi_{i,p}$ as a B-spline basis function.

Geometric mapping. B-splines and NURBS are used to build computational domains Ω in the physical space $\mathbb{R}^d$. In this paper, we specifically consider the case in which the parameter and physical spaces coincide (i.e. these being $\mathbb{R}^d$); we refer instead the interested reader to e.g. [1, 12, 13, 20, 21, 22] for NURBS mappings into lower-dimensional manifolds as curves and surfaces and their application in the IGA context. The geometric mapping is obtained by associating to each basis function $\psi_{i,p}$ a *control point* $\mathbf{P}_i \in \mathbb{R}^d$ for all $i = 1, \dots, N_b$, such that every point $\mathbf{x}$ of the *physical domain* Ω is obtained as

$$\mathbf{x}(\boldsymbol{\xi}) = \sum_{i=1}^{N_b} \mathbf{P}_i \, \psi_{i,p}(\boldsymbol{\xi}). \tag{28}$$

We assume that the previous mapping is invertible a.e. in $\widehat{\Omega}$; for this reason, given a generic function $v(\boldsymbol{\xi})$ defined in $\widehat{\Omega}$, we will indifferently write it in the physical domain Ω with the same notation $v(\mathbf{x})$. We finally remark that the mapping (28) determines the mesh $\mathcal{T}_h$ in the physical domain Ω from the corresponding one in the parameter domain $\widehat{\Omega}$ (see Fig. 3).

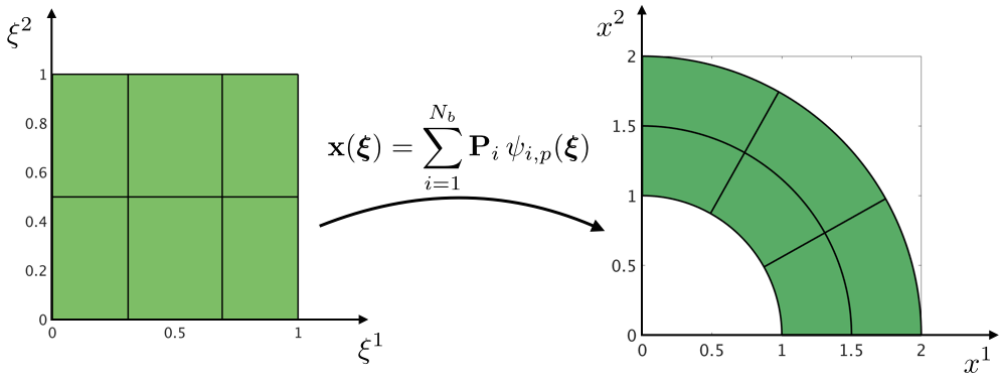

Figure 3: NURBS mapping from the parametric domain $\hat{\Omega}$ into the physical domain Ω

Formulation. We consider now the Isogeometric approximation of problem (2) according to the *isogeometric* concept for which the basis functions used to build the computational domain Ω are then used also to build the trial function space for the approximate solution. Let us set

$$S_\delta^k = span\{\psi_{i,p},\ i = 1, \ldots, N_b\} \tag{29}$$

and

$$V_\delta^k = V \cap S_\delta^k. \tag{30}$$

As for SEM, δ is an abridged notation now accounting for the mesh size (related to the number of distinct knots along each parametric direction) and the local polynomial degree p. We indicate with IGA-C^k the isogeometric approximation with globally C^k-continuous basis functions in the computational domain. If, in particular, the partition $\mathcal{T}_h$ induced by the knot vector Z^d is the same for both SEM and IGA, the finite dimensional space S_δ^0 of IGA-C^0 coincides with the finite dimensional space X_δ of SEM (see (7)) and then $V_\delta^0 = V_\delta$.

Let $\widetilde{g}_{k,\delta} \in S_\delta^k$ denote any discrete approximation of the lifting $\widetilde{g}$. The IGA-C^k approximation of (2) reads: find $u_{k,\delta} = (u_{k,\delta}^0 + \widetilde{g}_{k,\delta}) \in S_\delta^k$ with $u_{k,\delta}^0 \in V_\delta^k$ such that

$$a(u_{k,\delta}^0, v_\delta) = \mathcal{F}(v_\delta) - a(\widetilde{g}_{k,\delta}, v_\delta) \qquad \forall v_\delta \in V_\delta^k. \tag{31}$$

The subscript k (as, e.g., in $u_{k,\delta}$) indicates that the IGA-C^k case is considered.

Algebraic form. The discrete solution $u_{k,\delta}$ is expanded with respect to the B-spline basis functions, i.e.

$$u_{k,\delta}(\mathbf{x}) = \sum_{i=1}^{N_b} \hat{u}_{k,i} \psi_{i,p}(\mathbf{x}). \tag{32}$$

The IGA-C^k stiffness matrix is defined by

$$(K_k)_{ij} = a(\psi_{j,p}, \psi_{i,p}), \qquad i,j = 1, \ldots, N_b, \tag{33}$$

while the IGA-C^k mass matrix is defined by

$$(M_k)_{ij} = (\psi_{j,p}, \psi_{i,p})_{L^2(\Omega)}, \qquad i,j = 1, \ldots, N_b. \tag{34}$$

Both M_k and K_k are symmetric positive definite (s.p.d.) matrices.

We write now the algebraic counterpart of (31). First we reorder the basis functions $\psi_{i,p}$ so that the first N_b^0 ones are those vanishing on $\partial\Omega$ and the function $\widetilde{g}_{k,\delta}$ can be written as

$$\widetilde{g}_{k,\delta}(\mathbf{x}) = \sum_{j=N_b^0+1}^{N_b} \widehat{\widetilde{g}}_{k,j}\psi_{j,p}(\mathbf{x}), \tag{35}$$

where the coefficents $\widehat{\widetilde{g}}_{k,j}$ are unknowns. A possible way to compute $\widetilde{g}_{k,\delta}$ consists in defining it as the unique function in S_δ^k that minimizes $\int_{\partial\Omega}(\widetilde{g}_{k,\delta} - \widetilde{g})^2$, i.e., recalling that $\widetilde{g}|_{\partial\Omega} = g$, $\widetilde{g}_{k,\delta}$ is the unique solution of

$$\int_{\partial\Omega} \widetilde{g}_{k,\delta}\psi_{i,p} = \int_{\partial\Omega} g\psi_{i,p} \qquad i = N_b^0 + 1, \ldots, N_b. \tag{36}$$

After setting $M_{k,\partial\Omega} = (\psi_{j,p}, \psi_{i,p})_{L^2(\partial\Omega)}$ (it is the mass matrix on the boundary), $\widetilde{\mathbf{g}}_k = [\widehat{\widetilde{g}}_{k,j}]_{j=N_b^0+1}^{N_b}$ and $\mathbf{g} = [\int_{\partial\Omega} g\psi_{i,p}]_{i=N_b^0+1}^{N_b}$, in view of (35), solving (36) is equivalent to solve the linear system

$$M_{k,\partial\Omega}\widetilde{\mathbf{g}}_k = \mathbf{g}.$$

Then we set $\mathbf{u}_k = [\hat{u}_{k,i}]_{i=1}^{N^0}$, $\mathbf{f}_k = [\hat{f}_{k,i}]_{i=1}^{N^0}$ with $\hat{f}_{k,i} = (f, \psi_{i,p})_{L^2(\Omega)}$ and $\mathbf{g}_k$ such that

$$(\mathbf{g}_k)_i = \sum_{j=N_b^0+1}^{N_b} (K_k)_{ij}\widehat{\widetilde{g}}_{k,j} \qquad \text{for } i = 1, \ldots, N_b^0,$$

so that the algebraic form of (31) reads: look for the solution $\mathbf{u}_k$ of

$$K_k\mathbf{u}_k = \mathbf{f}_k - \mathbf{g}_k, \tag{37}$$

where we understand that K_k is restricted to the rows $i = 1, \ldots, N_b^0$ and the columns $j = 1, \ldots, N_b^0$.

Error estimates. Under the assumption that $g = 0$ on $\partial\Omega$ and that the partition defined by the knot vector Z is locally quasi uniform, that is, there exists a constant $\theta \geq 1$ such that the mesh sizes $h_i = \zeta_{i+1} - \zeta_i$ satisfy the relation $\theta^{-1} \leq h_i/h_{i+1} \leq \theta$ for $i = 0, \ldots, n-1$, in [11, Thm. 3.4 and Cor. 4.16] it is proved that there exists a positive constant $c = c(s, p, \theta)$ independent of $h = \max_i h_i$ such that, for any $0 \leq r \leq s \leq p+1$,

$$\|u - u_{k,\delta}\|_{H^r(\Omega)} \leq ch^{\min(s,p+1)-r}\|u\|_{H^s(\Omega)} \qquad \forall u \in H^s(\Omega). \tag{38}$$

This is an optimal convergence estimate for IGA with respect to h (h-refinement) for all values of $k = 0, \ldots, p-1$; see also [25].

The convergence rate of IGA with respect to both p and k was studied in [10] when $p \geq 2k+1$. We warn the reader that in our paper the parameter k is used to identify the C^k regularity of the B-spline basis functions (and then of the IGA solution), whereas in [10] it denotes the Sobolev regularity of the IGA solution. In order to avoid misunderstandings, we denote by k_b the index k used in [10], whence $k_b = k + 1$.

Let us now consider the case of univariate B-splines. For any $k_b \geq 0$ integer, in [10] the authors introduce a projection operator $\hat{\pi}_{p,k_b} : H^{k_b}(\Lambda) \to \mathbb{P}_p(\Lambda)$, where $\Lambda = (-1, 1)$, while $\mathbb{P}_p(\Lambda)$ is the space of the restrictions to Λ of polynomials of degree almost p, such that

$$(\hat{\pi}_{p,k_b} u)^{(j)}(\pm 1) = u^{(j)}(\pm 1), \qquad j = 0, \ldots, k_b - 1. \tag{39}$$

$\hat{\pi}_{p,k_b}$ is not the orthogonal projection operator from $H^{k_b}(\Lambda)$ to $\mathbb{P}_p(\Lambda)$, nevertheless it is a projection operator that perserves the values of the function and of its derivatives up to order $k_b - 1$ at the end-points of Λ. Moreover (see [10, Cor. 2 and Lemma 4]), if $u : \Lambda \to \mathbb{R}$ with $u^{(k_b)} \in H^s(\Lambda)$, if $p \geq 2k_b - 1$ and $s \leq p - k_b + 1$, then for any $j = 0, \ldots, k_b$ it holds

$$\|u^{(j)} - (\hat{\pi}_{p,k_b} u)^{(j)}\|_{L^2(\Lambda)} \leq C \left(\frac{e}{2}\right)^{s+k_b-j} (p - k_b + 1)^{-(s+k_b-j)} |u^{(k_b)}|_{H^s(\Lambda)}. \tag{40}$$

By introducing the linear continuous mappings $F_i : \Lambda \to I_i = (\zeta_i, \zeta_{i+1})$, for $i = 0, \ldots, n-1$ (such that $F_i(\xi) = \xi(\zeta_{i+1} - \zeta_i)/2 + (\zeta_{i+1} + \zeta_i)/2$), we define the global projection operator $\pi_{p,k_b} : H^{k_b}(0, 1) \to S_\delta^{(k_b-1)}$ by the relations

$$(\pi_{p,k_b} u) \circ F_i = \hat{\pi}_{p,k_b}(u \circ F_i), \qquad i = 1, \ldots, n-1. \tag{41}$$

For any $u \in H^{k_b}(0, 1)$, $\pi_{p,k_b} u$ preserves the values of u and of all its derivatives up to order $k_b - 1$ at the knots ζ_i, for $i = 0, \ldots, n$. If the partition induced by the knot vector Z is uniform with size h, then ([10, Thm. 2])

$$\|u - \pi_{p,k_b} u\|_{H^j(0,1)} \leq C h^{\sigma-j} (p - k_b + 1)^{-(\sigma-j)} |u|_{H^\sigma(0,1)} \qquad \forall u \in H^\sigma(0, 1), \tag{42}$$

for any $j = 0, \ldots, k_b$, for $k_b \leq \sigma \leq p + 1$, and $p \geq 2k_b - 1$, with C independent of σ, j, h, p and k_b. Thus, recalling that $k_b = k + 1$ and thanks to (42) and to the Céa's Lemma, it holds

$$\|u - u_{k,\delta}\|_{H^j(0,1)} \leq C h^{\sigma-j} (p - k)^{-(\sigma-j)} |u|_{H^\sigma(0,1)}, \tag{43}$$

for $0 \leq j \leq k + 1 \leq \sigma \leq p + 1$ and $p \geq 2k + 1$, i.e. the convergence of IGA is optimal also w.r.t. to p and k.

In the following theorem we extend the convergence estimate (43) to any $\sigma \geq k+1$ and without the upper bound $\sigma \leq p + 1$ that was instead essential to prove (40). In this way, the convergence rate w.r.t. p exploits the whole regularity order of the exact solution.

Theorem 1. *Let $d = 1$, $p \geq 1$ and $k \geq 0$ be two integers with $p \geq 2k + 1$, and let $u_{k,\delta} \in V_\delta^k$ be the solution of (31). Let the solution u of (2) belong to $H^s(\Omega)$ with $s \geq k + 1$. Then, if the partition induced by the knot vector Z is uniform of size h, for any real numbers r and s with $0 \leq r \leq k + 1 \leq s$, it holds*

$$\|u - u_{k,\delta}\|_{H^r(0,1)} \leq C h^{s-r} (p - k + 1)^{-(s-r)} \|u\|_{H^s(0,1)}, \tag{44}$$

with C independent of both h and p.

Proof. The result follows from the argument used in [4, Sect.6], however we report here a sketch of the proof for reader's convenience.

Let $k_b \geq 1$ and $p \geq 2k_b - 1$ be two integers. First, we consider the orthogonal projection operator $\pi_p^{k_b,0} : H^s(\Lambda) \cap H_0^{k_b}(\Lambda) \to \mathbb{P}_p^{k_b,0}(\Lambda) = \mathbb{P}_p(\Lambda) \cap H_0^{k_b}(\Lambda)$, that satisfies (see the proof of Theorem 6.2 of [4])

$$\|u - \pi_p^{k_b,0} u\|_{H^r(\Lambda)} \leq c(p - k_b)^{r-s} \|u\|_{H^s(\Lambda)} \qquad \forall u \in H^s(\Lambda) \cap H_0^{k_b}(\Lambda), \tag{45}$$

with $0 \leq r \leq k_b \leq s$ and the constant c independent of p. Then, we introduce the set of polynomials $\chi_{k_b,\ell}$, $0 \leq \ell \leq k_b - 1$ such that $\chi_{k_b,\ell} \in \mathbb{P}_{2k_b-1}(\Lambda)$ is the unique polynomial satisfying the following conditions

$$\begin{aligned} &\chi_{k_b,\ell}^{(\ell)}(-1) = 1, \qquad \chi_{k_b,\ell}^{(m)}(-1) = 0, \quad 0 \leq m \leq k_b - 1,\ m \neq \ell, \\ &\chi_{k_b,\ell}(1) = \chi'_{k_b,\ell}(1) = \cdots = \chi_{k_b,\ell}^{(k_b-1)}(1) = 0; \end{aligned}$$

then, we define the polynomial

$$\chi_{k_b}(\zeta) = \sum_{\ell=0}^{k_b-1} u^{(\ell)}(-1)\chi_{k_b,\ell}(\zeta) + \sum_{\ell=0}^{k_b-1} (-1)^\ell u^{(\ell)}(1)\chi_{k_b,\ell}(-\zeta) \tag{46}$$

and the function $\tilde{u}_{k_b} = u - \chi_{k_b} \in H_0^{k_b}(\Lambda)$.

The projection operator $\widetilde{\pi}_p^{k_b} : H^{k_b}(\Lambda) \to \mathbb{P}_p(\Lambda)$ is defined for any $k_b \geq 1$ and $p \geq 2k_b - 1$ by

$$\widetilde{\pi}_p^{k_b} u = \pi_p^{k_b,0} u + \chi_{k_b}; \tag{47}$$

it preserves the values of the function and of its derivatives of order up to $k_b - 1$ at the end-points of Λ. Thanks to (47) it holds

$$u - \widetilde{\pi}_p^{k_b} u = \tilde{u}_{k_b} - \pi_p^{k_b,0} \tilde{u}_{k_b}; \tag{48}$$

in this manner, by using (45) and by recalling that the map $u \mapsto \tilde{u}_{k_b}$ is continuous in $H^s(\Lambda)$ (see [4, formula (6.19)]), we have

$$\|u - \widetilde{\pi}_p^{k_b} u\|_{H^r(\Lambda)} \leq c(p - k_b)^{r-s} \|u\|_{H^s(\Lambda)} \qquad \forall u \in H^s(\Lambda) \tag{49}$$

for any integer $k_b \geq 1$ and $p \geq 2k_b - 1$ and for any real numbers r and s such that $0 \leq r \leq k_b \leq s$, with c independent of p.

By using the linear mappings F_i introduced above and starting from $\widetilde{\pi}_p^{k_b}$, we define a global projection operator $\pi_p^{k_b} : H^{k_b}(0,1) \to S_\delta^{(k_b-1)}$ that preserves the values of u and its derivatives up to order $k_b - 1$ at the end-points of each interval I_i. By using the uniform distribution of the knot vector Z and by standard scaling arguments it holds

$$\|u - \pi_p^{k_b} u\|_{H^r(0,1)} \leq C h^{\min(p+1,s)-r} (p - k_b)^{r-s} \|u\|_{H^s(0,1)} \qquad \forall u \in H^s(0,1), \tag{50}$$

with $0 \leq r \leq k_b \leq s$ and c independent of both h and p.

By setting $k = k_b - 1$ and thanks to Céa's Lemma, the thesis follows. □

The analysis in the case $d = 1$ and $p \leq 2k + 1$ still remains open [11, Remark 4.18].

The analysis for the case $d = 2$ is addressed in [4, Sect. 7] and in [10]. In particular, referring to [10], if $Q = \Lambda^2 = (-1,1)^2$, if the partition induced by the knot vector $Z \times Z$ is uniform, and if the same values of p and k are used along the two directions, then ([10, Cor. 8])

$$\|u - u_{k,\delta}\|_{H^\ell(Q)} \leq c h^{\sigma-\ell} (p - k)^{-(\sigma-\ell)} \|u\|_{H^\sigma(Q)} \qquad \forall u \in H^\sigma(Q), \tag{51}$$

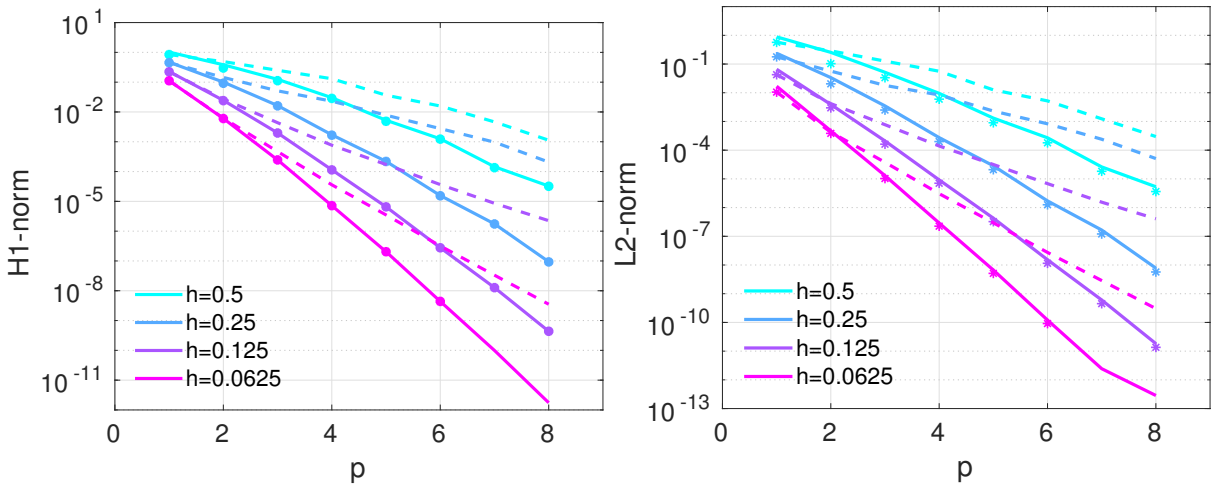

Figure 4: *Cube domain test case.* Errors $e_{\delta,1}$ (H^1-norm (left)) and $e_{\delta,0}$ (L^2-norm (right)) vs. the polynomial degree p. Markers refer to IGA-C^0 solution, dashed lines to IGA-C^{p-1} solution, while the continuous lines to SEM-NI solution. The color identifies the mesh size h for all the approaches

for any $0 \leq \ell \leq k+1$, provided that $2k+2 \leq \sigma \leq p+1$. Moreover, the positive constant c is independent of σ, ℓ, h, p and k.

When $d = 3$, by assuming again that p and k are the same along all directions, the more restrictive condition $3k+3 \leq \sigma \leq p+1$ should be assumed to prove an analogous estimate (see [10, Remark 1, pag. 300] and [4, Remark 7.1]).

3. Accuracy: numerical tests

In this section we compare the convergence rates of the errors under h- and p-refinement of IGA and SEM-NI methods. We remark that for the IGA-C^{p-1} case, the $p-$refinement coincides with the k-refinement procedure typical of NURBS-based IGA [9, 14]. We consider only the case $d = 3$; we omit to show numerical results for $d = 1$ and $d = 2$ since the methods behave similarly.

3.1. Cube domain

We consider problem (1) in $\Omega = (0,1)^3$ and we choose the right hand side f and the Dirichlet datum g so that the exact solution is

$$u(\mathbf{x}) = \sin(4\pi\,\mathrm{x}\,\mathrm{y}\,\mathrm{z})\sin(4\pi\,(\mathrm{x}-1)(\mathrm{y}-1)(\mathrm{z}-1)). \tag{52}$$

Then, we solve it by means of IGA-C^0, IGA-C^{p-1} and SEM-NI on a set of uniform meshes of size h and with local polynomial degree p. We recall that, if $ne_{h,1}$ is the number of elements along each direction, then $h = 1/ne_{h,1}$ for all the methods.

First, we choose $h \in \{1/16, 1/8, 1/4, 1/2\}$ and $p = 1, \ldots, 8$ and we analyse the behavior of the errors versus either h or p.

Then we analyse the behavior of the errors versus the total number *dof* of degrees of freedom and finally versus the number *nnz* of non-zero entries of the stiffness matrices for several values of p and h that we specify in the sequel.

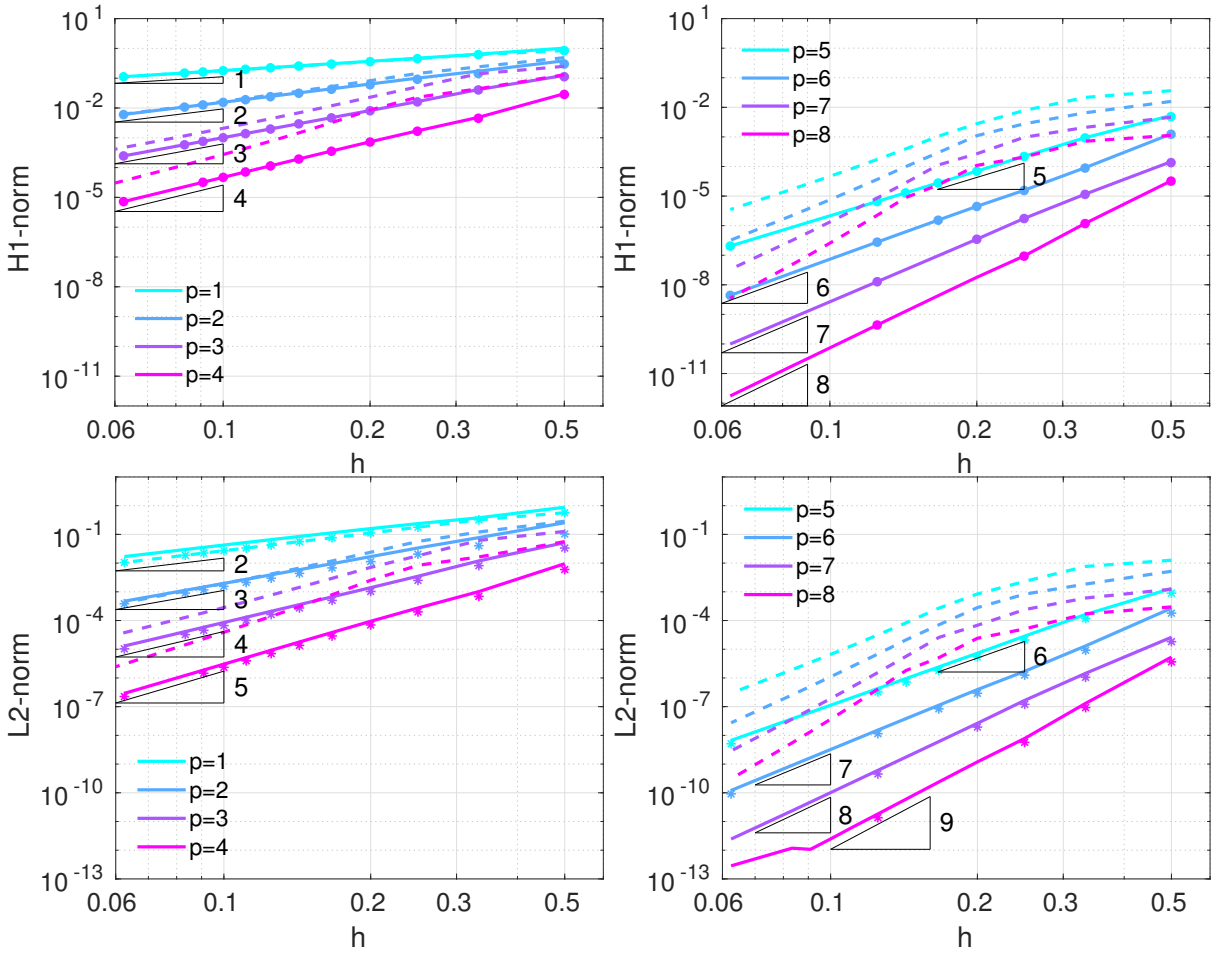

Figure 5: *Cube domain test case.* Errors $e_{\delta,1}$ (H^1-norm, (top)) and $e_{\delta,0}$ (L^2-norm (bottom)) vs. the mesh size h. Markers refer to IGA-C^0 solution, dashed lines to IGA-C^{p-1} solution, while continuous lines to SEM-NI solution. The color identifies the polynomial degree p for all the approaches

Error vs. h and p. In Figure 4 we show the H^1-norm (at left) and the L^2-norm (at right) of the relative errors between the numerical solutions (obtained by one of the three methods IGA-C^0, IGA-C^{p-1} and SEM-NI) and the exact solution (52), vs. the polynomial degree p, with h fixed. More precisely, we set

$$e_{\delta,1} = \frac{\|u - u_\delta\|_{H^1(\Omega)}}{\|u\|_{H^1(\Omega)}}, \qquad e_{\delta,0} = \frac{\|u - u_\delta\|_{L^2(\Omega)}}{\|u\|_{L^2(\Omega)}}. \tag{53}$$

The H^1-norm of the IGA-C^0 and SEM-NI errors almost coincide: as we can see in both pictures of Figure 4, the markers (that represent the errors for IGA-C^0) are overlapped with the continuous lines (that represent the errors for SEM-NI). The errors of IGA-C^{p-1} (dashed lines) exhibit the slowest decay rates.

The exact solution we are considering belongs to $C^\infty(\Omega)$, thus (in view of the estimates (20) and (44), suitably extended to the case $d = 3$) the errors of IGA-C^0 and SEM-NI decay with

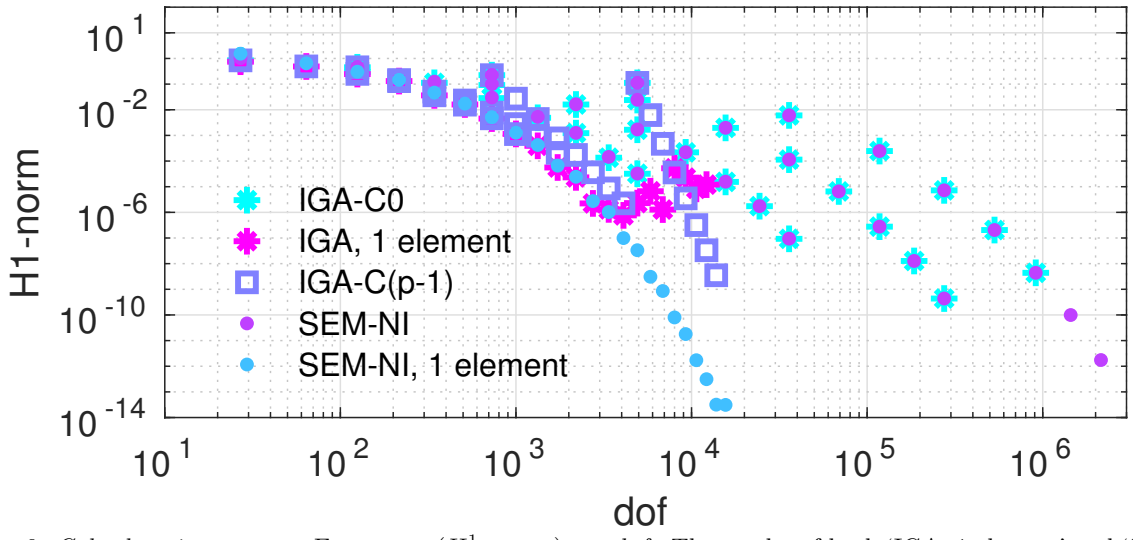

Figure 6: *Cube domain test case.* Errors $e_{\delta,1}$ (H^1-norm) vs. dof. The results of both 'IGA, 1 element' and 'SEM-NI, 1 element' are obtained with $ne_{h,1} = 1$ and $p = 1, \ldots, 24$, while those of IGA-C^0, IGA-C^{p-1} and SEM-NI are computed with $ne_{h,1} \in \{2, 4, 8, 16\}$ and $p = 1, \ldots, 8$

respect to p faster than any algebraic power of p, i.e. exponentially with respect to p. The same happens for IGA-C^{p-1}, although the rate of decay of the error is slower than that of IGA-C^0. The L^2-norm of the errors for IGA-C^0 is slightly lower than the corresponding SEM-NI errors.

In Figure 5 we show the H^1-norm (top) and the L^2-norm (bottom) of the errors (53) versus the mesh size h, when p is fixed. Optimal convergence rates are shown by all the methods.

Error vs dof. The total number of degrees of freedom (dof) of the discretization is a function of both the local polynomial degree p and the global number of mesh elements ne_h. In the case in which the partition $\mathcal{T}_h$ is quasi uniform and tensor-based, we denote by $ne_{h,1} = c/h$ (c is a constant that depends only on Ω) the number of elements along any spatial direction, so that the global number of elements is $ne_h = (ne_{h,1})^d$ and the global number of degrees of freedom dof (including those associated with the boundary) is:

	IGA-C^0	IGA-C^{p-1}	SEM-NI (or SEM)
dof	$(ne_{h,1}p + 1)^d$	$(p + ne_{h,1})^d$	$(ne_{h,1}p + 1)^d$.

We notice that the number of degrees of freedom of IGA-C^0 coincides with that of SEM-NI, while that of IGA-C^{p-1} grows more slowly.

In Figures 6 and 7 the H^1-norm and the L^2-norm of the errors are plotted against dof. We considered several values of p and of $ne_{h,1}$. The choice of both of them is limited by the RAM capacity (16 GBytes) of the hardware used to perform the numerical simulations.

When $ne_h = ne_{h,1} = 1$, the numerical solutions are global polynomials in the computational domain for all the three methods. IGA-C^0 and IGA-C^{p-1} provide the same solution (named simply IGA in Figures 6 and 7) and their errors spectrally decay w.r.t. p until $p = 13$; then, rounding errors downgrade the convergence and the H^1-norm error remains up to 10^{-6} for $p \geq 13$. The round-off errors are amplified by the large condition number of the IGA stiffness matrix when $h = 1$ (see Tab. 3 in Sect. 4).

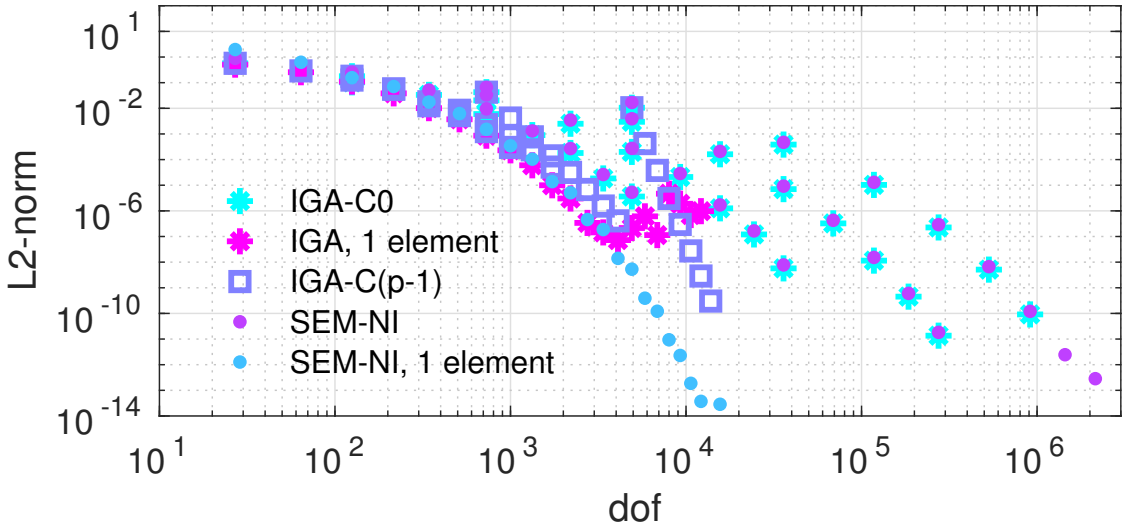

Figure 7: *Cube domain test case.* Errors $e_{\delta,0}$ (L^2-norm) vs. dof. The results of both 'IGA, 1 element' and 'SEM-NI, 1 element' are obtained with $ne_{h,1} = 1$ and $p = 2, \ldots, 24$, while those of IGA-C^0, IGA-C^{p-1} and SEM-NI are computed with $ne_{h,1} \in \{2, 4, 8, 16\}$ and $p = 1, \ldots, 8$

On the contrary, the SEM-NI error vs. p decays until it is quite close to the machine precision 10^{-14}. The same behavior is also observed for the L^2-norm error.

For a fixed $ne_{h,1} > 1$, the error of IGA-C^{p-1} vs. $dof = dof(p)$ decays faster than the errors of both IGA-C^0 and SEM-NI. Nevertheless, in the range of $p \leq 8$ and $2 \leq ne_{h,1} \leq 16$, the minimum error measured for IGA-C^{p-1} is about 10^{-9}, obtained with $ne_{h,1} = 16$ and $p = 8$ (for which $dof = 15625$); larger values of these discretization parameters produce matrices too large and too dense to be stored into the 16GB RAM of the hardware used for the numerical simulations. In the same range of $p \leq 8$ and $2 \leq ne_{h,1} \leq 16$, the minimum error reached by SEM-NI is about 10^{-12} (obtained with $ne_{h,1} = 16$ and $p = 8$, for which $dof = 2146689$). We speculate that also IGA-C^0 would reach the minimum error provided by SEM-NI with $ne_{h,1} = 16$ and $p = 8$, but the RAM capacity of 16 GBytes limited the runs of IGA-C^0 to $p = 6$ when $ne_{h,1} = 16$.

Matrix sparsity pattern. As it emerges from the previous considerations, dof is not the unique reference parameter to be taken into account in measuring the efficiency of a method. As a matter of fact, other important issues, especially for $d = 3$, are the sparsity pattern of the stiffness matrix and its *number of nonzero entries*, say nnz. The latter is a measure not only of the memory space required to store the matrix, but also of the computational complexity that must be addressed, first of all to assemble the stiffness matrix and then to solve the linear system.

The numerical results shown in these sections have been produced using an Intel(R) Core(TM) i7-4790 CPU @ 3.60GHz with 4 Cores and 16GB of RAM. When $d = 3$, starting from moderate values of p (e.g. $p = 4$) and moderate values of $ne_{h,1}$ (e.g. $ne_{h,1} = 8$) the direct solution of both the SEM-NI linear system (15) and the IGA-C^0 system (37) become prohibitive on this hardware. This is due to the fill-in that occurs during the elimination process involved in the direct solver.

As a consequence, a preconditioned iterative method, like, e.g., Krylov ones, is in order. We solve the linear systems by the Bi-GCStab method [26], preconditioned by an incomplete LU factorization. On our machine, the iterative numerical solution of the linear system of IGA-C^0 becomes prohibitive for $p > 4$ and $ne_{h,1} > 7$.

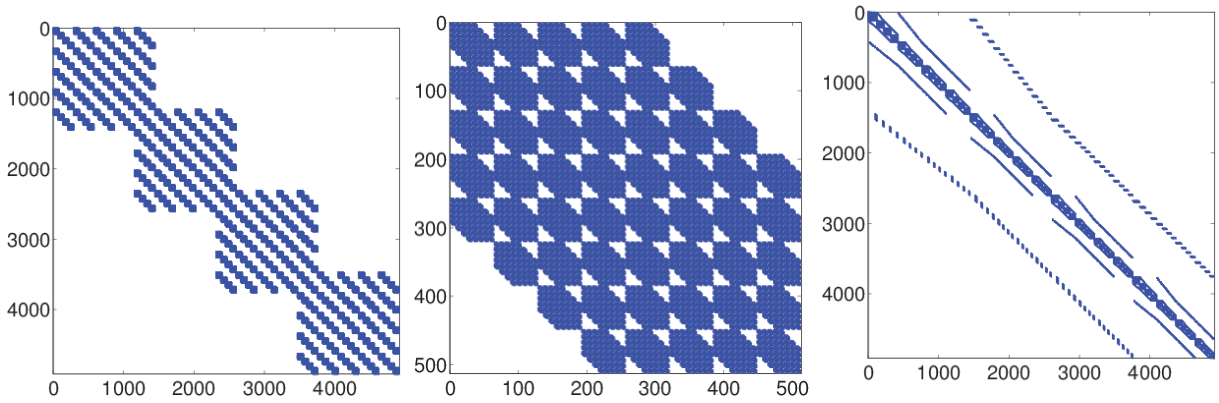

Figure 8: Pattern of the stiffness matrix of IGA-C^0 (left), IGA-C^{p-1} (center), and SEM-NI (right) when $\Omega = (0,1)^3$, $p = 4$ and $ne_{h,1} = 4$. dof is 4913 for both IGA-C^0 and SEM-NI, while it is 512 for IGA-C^{p-1}. nnz is 911599 for IGA-C^0, 140604 for IGA-C^{p-1}, and 46575 for SEM-NI. The fill-in percentage are 2% for SEM, 4% for IGA-C^0 and 54% for IGA-C^{p-1}

We notice that, even if both the IGA and SEM-NI stiffness matrices are symmetric and positive definite for the problem at hand, we used the Bi-GCStab instead of the Conjugate Gradient method. As a matter of fact, since the condition number of the IGA stiffness matrices heavily grows with p (see the Sect. 4), the symmetric incomplete Cholesky factorization breaks down when computing the square root of non-positive values. At each iteration of the Krylov method, one has to compute matrix-vector products (whose computational cost is proportional to nnz) and to solve auxiliary linear systems related to the preconditioner. We omit here the analysis of the costs associated with the preconditioner, that is out of the scope of this paper.

In the next subsection we provide a comparison of the computational cost for assembling the stiffness matrix of IGA-C^{p-1} and SEM-NI versus both dof and nnz in the more realistic case of a domain with curved boundary. Here we just plot the H^1–norm error versus the parameter nnz.

In Fig. 8 the pattern of the stiffness matrix stemming from the three methods are shown, for the case $p = 4$ and $ne_{h,1} = 4$, when $d = 3$ and $\Omega = (0,1)^3$. We notice that, in the case of SEM-NI, nnz is independent of the fact that quadrature formulas are used to approximate integrals; indeed, the same sparsity pattern would be obtained if one uses exact integration instead of the numerical one.

Then, in Figure 9 we show the H^1-norm of the error versus nnz. SEM-NI is the method (among the three) that provides the minimum errors for a prescribed value of nnz.

3.2. Domain with curved boundary: one-eight of the sphere

In this section we compare the accuracy of SEM-NI and IGA (limited to the more interesting case IGA-C^{p-1}) by solving the Poisson problem in a computational domain with curved boundary.

Let Ω be one-eight of the sphere centered at the origin and with radius equal to one, i.e. $\Omega = \{\mathbf{x} = (\mathrm{x}, \mathrm{y}, \mathrm{z}) \in \mathbb{R}^3 : \ \mathrm{x} \geq 0, \ \mathrm{y} \geq 0, \ \mathrm{z} \geq 0, \ \mathrm{x}^2 + \mathrm{y}^2 + \mathrm{z}^2 \leq 1\}$.

We look for the solution of the differential problem (1) with $g(\mathbf{x})$ and $f(\mathbf{x})$ such that the exact solution is $u(\mathbf{x}) = \mathrm{y}\,\mathrm{z}\,\exp(-\mathrm{x}^2 - \mathrm{y}^2 - \mathrm{z}^2)$.

SEM-NI discretization. In order to approximate the solution of (1) by SEM-NI we partition the computational domain Ω into hexaedra. The coarsest decomposition we consider is made of four hexaedra as shown in Fig. 10, left, such decomposition ensures that the transfinite mappings

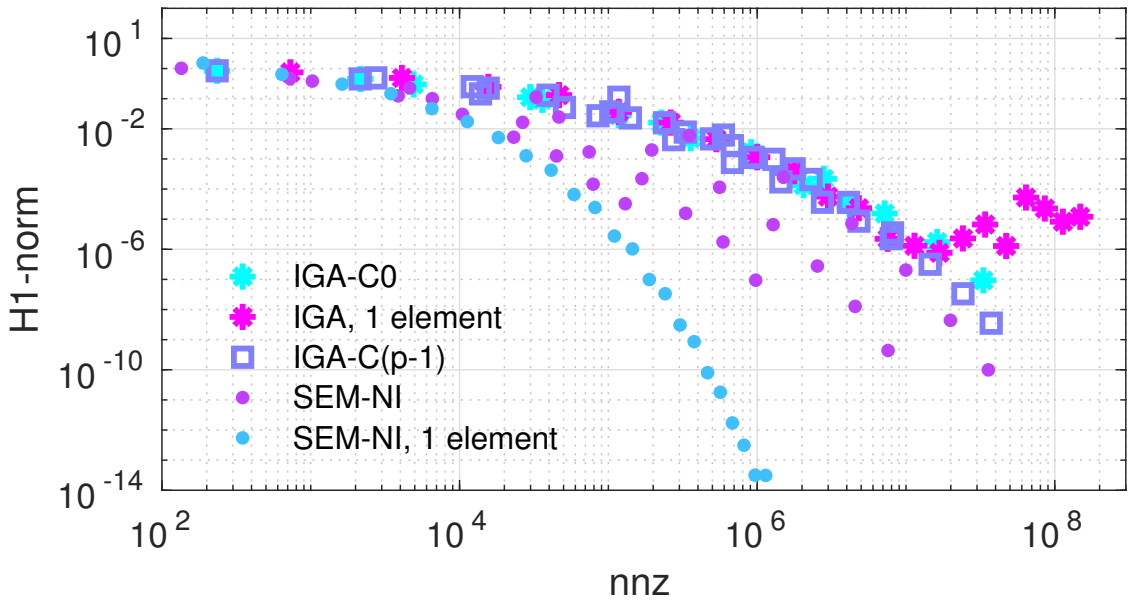

Figure 9: *Cube domain test case.* H^1-norm of the error versus the non-zero entries of the stiffness matrix when $\Omega = (0,1)^3$

Table 1: *One-eight of the sphere test case.* SEM-NI discretization parameters. The total number of spectral elements is $ne_h = ne_{h,1}^3 \times 4$. dof is the number of degrees of freedom internal to Ω

		dof					
$ne_{h,1}$	ne_h	$p=1$	$p=2$	$p=3$	$p=4$	$p=5$	$p=6$
1	4	1	13	157	1597	5853	14461
2	32	13	157	1597	14461	50877	123133
4	256	57	621	5853	50877	176541	424317
8	2048	157	1597	14461	123133	424317	1016317
12	6912	337	3277	28957	243517	835677	1997437
16	16384	621	5853	50877	424317	1452093	3465981

$\mathbf{F}_\ell$ introduced in Sect. 2.1 are invertible. Then, in each of these four hexaedra we consider $ne_{h,1} \times ne_{h,1} \times ne_{h,1}$ uniform hexaedra spectral elements T_ℓ (see Sect. 2.1) with $ne_{h,1} = 1, 2, 4, 8, 12, 16$. The global number of elements is $ne_h = 4 \cdot (ne_{h,1})^3$. In each element T_ℓ the local polynomial degree p along any spatial direction ranges from 1 to 16 when $ne_{h,1} = 1$, from 1 to 8 when $ne_{h,1} = 2,\ 4,\ 8$, and from 1 to 6 when $ne_{h,1} = 12,\ 16$. The total number of degrees of freedom dof internal to Ω are shown in Table 1 for $p = 1, \ldots, 6$.

IGA discretization. We consider IGA-C^{p-1} in a single NURBS patch (see Fig. 11), with $ne_{h,1} = 2, 4, 8, 12, 16$ and different values of p, more precisely: p ranges from 1 to 15 when $ne_{h,1} = 2$, from 1 to 13 when $ne_{h,1} = 4$, from 1 to 10 when $ne_{h,1} = 8$, and from 1 to 8 when $ne_{h,1} = 12,\ 16$. The global number of degrees of freedom internal to Ω is shown in Table 2.

The IGA numerical solutions for this test case have been computed by GeoPDEs 3.0, a package for Isogeometric Analysis written in Matlab and Octave ([27]), while SEM-NI numerical solutions have been computed using a proprietary software written in Matlab and Octave.

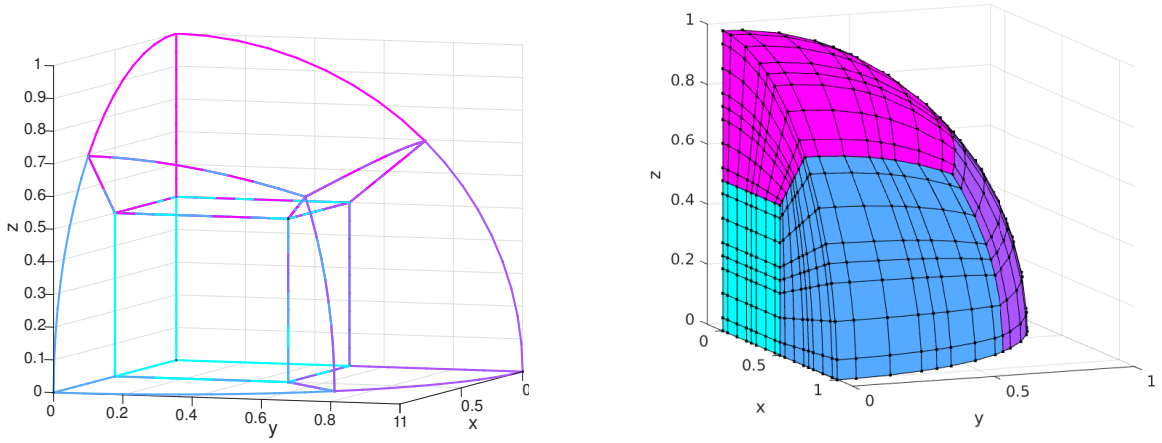

Figure 10: *One-eight of the sphere test case.* The coarsest decomposition of Ω in 4 hexahedra used for the SEM-NI approximation (left); a finer Spectral Element decomposition with $ne_{h,1} = 2$ and $p = 4$ (right), for which the global number of spectral elements is $ne_h = 2^3 \times 4$

Table 2: *One-eight of the sphere test case.* IGA-C^{p-1} discretization parameters. The total number of elements is $ne_h = ne_{h,1}^3$, dof is the number of degrees of freedom internal to Ω

		dof					
$ne_{h,1}$	ne_h	$p=1$	$p=2$	$p=3$	$p=4$	$p=5$	$p=6$
2	8	1	8	64	512	1728	4096
4	64	8	27	125	729	2197	4913
8	512	27	64	216	1000	2744	5832
12	1728	64	125	343	1331	3375	6859
16	4096	125	216	512	1728	4096	8000

The H^1–norm errors $e_{\delta,1}$ (see definition (53)) are shown in Figures 12–14 for both SEM-NI and IGA-C^{p-1} discretizations versus the polynomial degree, the number of mesh elements and the total number of degrees of freedom. The errors decay exponentially w.r.t. the polynomial degree p for both SEM-NI and IGA-C^{p-1}; as in the test case on the cube domain, the SEM-NI errors decay faster than the IGA-C^{p-1} ones. Optimal convergence w.r.t. the mesh size h is confirmed for both the methods.

As we can appreciate in Fig. 14, the IGA-C^{p-1} errors decay faster than the SEM-NI ones when we analyse the behavior vs. the number dof of degrees of freedom, nevertheless the curve of the errors obtained with SEM-NI and $ne_{h,1} = 1$ (for which the global number of elements is $ne_h = 4$) is the lower one and the errors computed with IGA-C^{p-1} stay above it for all the combinations of p and ne_h allowed by the 16GB RAM of our computer.

In Figures 15 and 16 we show the CPUtimes (in seconds) needed to assemble the stiffness matrix versus dof and nnz, respectively. We verified that, for both IGA-C^{p-1} and SEM-NI, the computational cost to assemble the stiffness matrix exceeds that required to solve the corresponding linear system. The CPUtimes needed to assemble the IGA-C^{p-1} stiffness matrix grow like $dof^{3.2}$

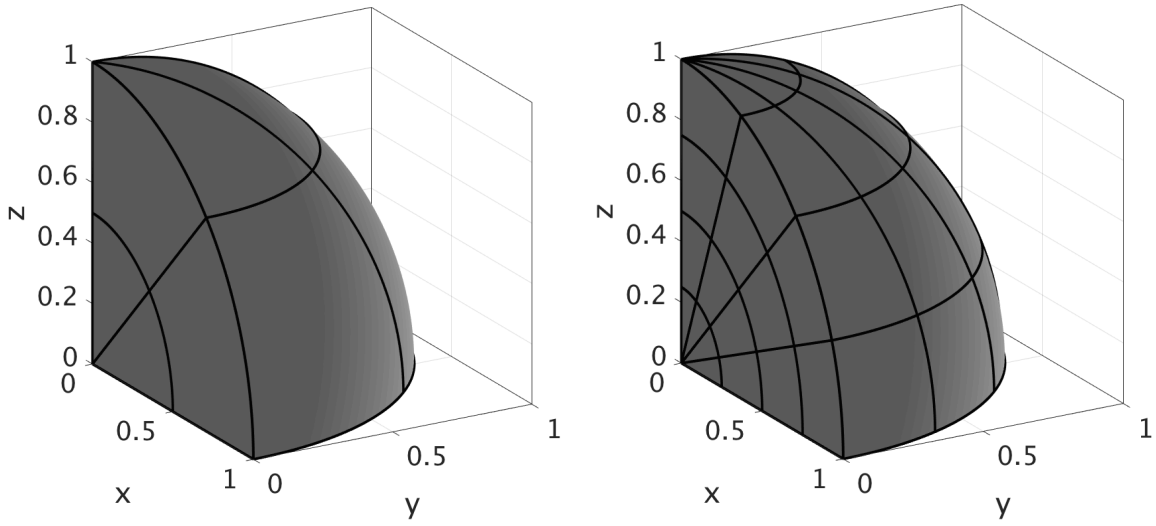

Figure 11: *One-eight of the sphere test case.* NURBS representation of the domain with $ne_{h,1} = 2$ and $p = 2$ (left) and $ne_{h,1} = 4$ and $p = 2$ (right)

and $nnz^{1.6}$, while in the case of SEM-NI they grow like $dof^{1.5}$ and nnz.

These results lead us to compare the errors of the two methods vs the number nnz of non-zeros entries of the stiffness matrices. In Fig. 17 the H^1–norm errors $e_{\delta,1}$ versus nnz are shown and finally, in Fig. 18, the H^1–norm errors $e_{\delta,1}$ vs the CPUtime needed to assemble the stiffness matrix are plotted. In order to reach a prescribed error, there exists at least one combination of p and $ne_{h,1}$ such that the computational cost of SEM-NI is lower than that of IGA-C^{p-1} and, viceversa, if our target is a small CPUtime, the SEM-NI error corresponding to that CPUtime is lower than the IGA-C^{p-1} one.

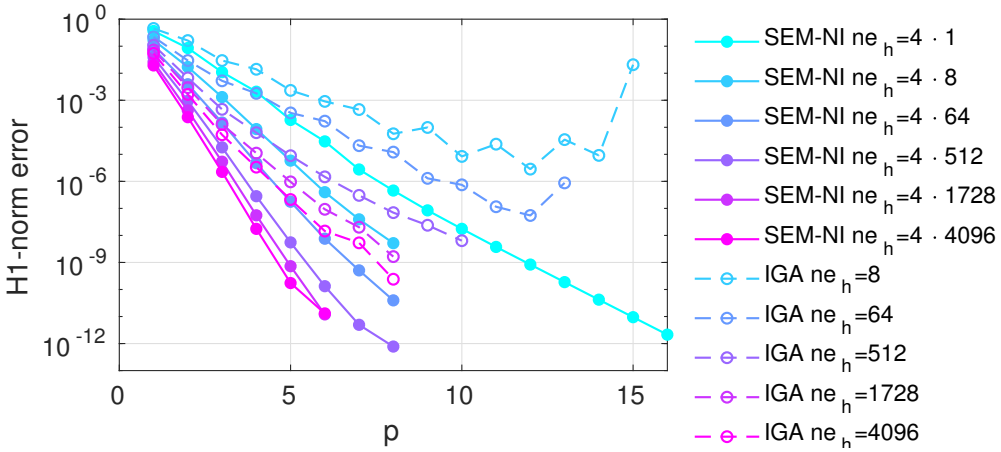

Figure 12: *One-eight of the sphere test case.* The discretization error $e_{\delta,1}$ (H^1–norm) versus the polynomial degree p. IGA in the legend stands for IGA-C^{p-1}

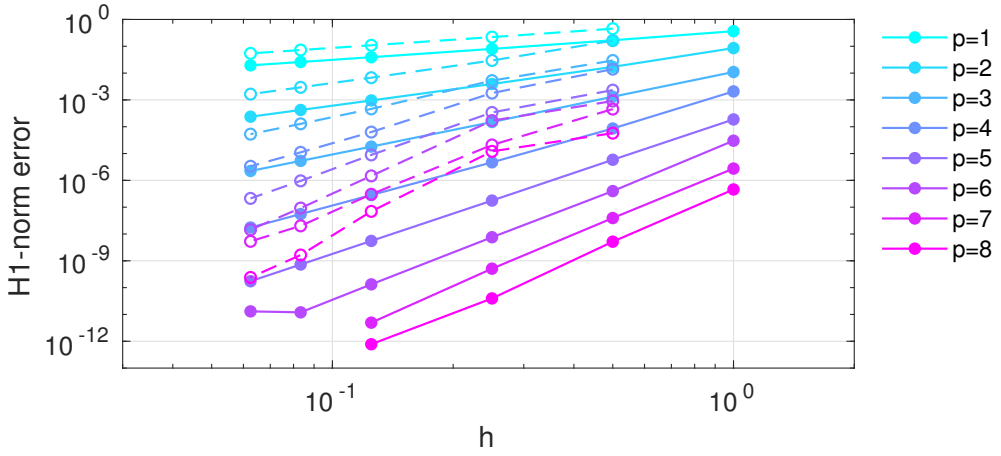

Figure 13: *One-eight of the sphere test case.* The discretization error $e_{\delta,1}$ (H^1–norm) versus the mesh size $h \simeq 1/ne_{h,1}$. IGA in the legend stands for IGA-C^{p-1}

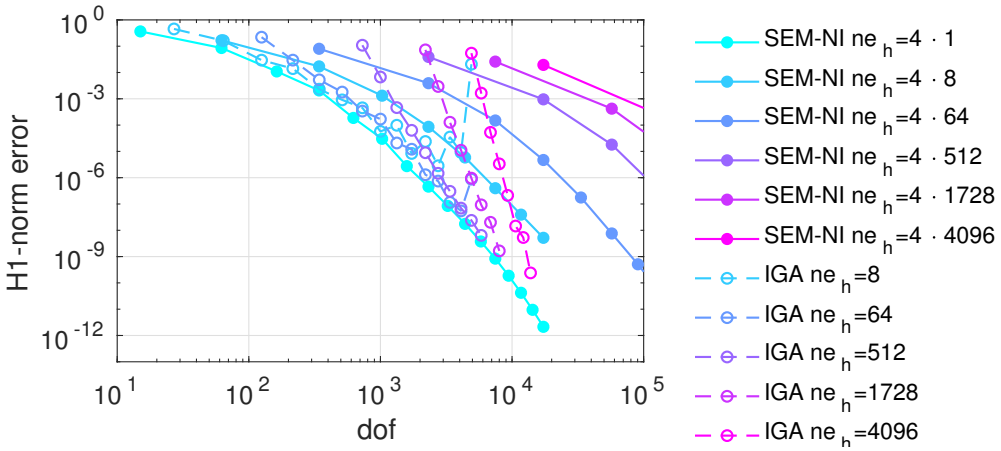

Figure 14: *One-eight of the sphere test case.* The discretization error $e_{\delta,1}$ (H^1–norm) versus the number of degrees of freedom. IGA in the legend stands for IGA-C^{p-1}

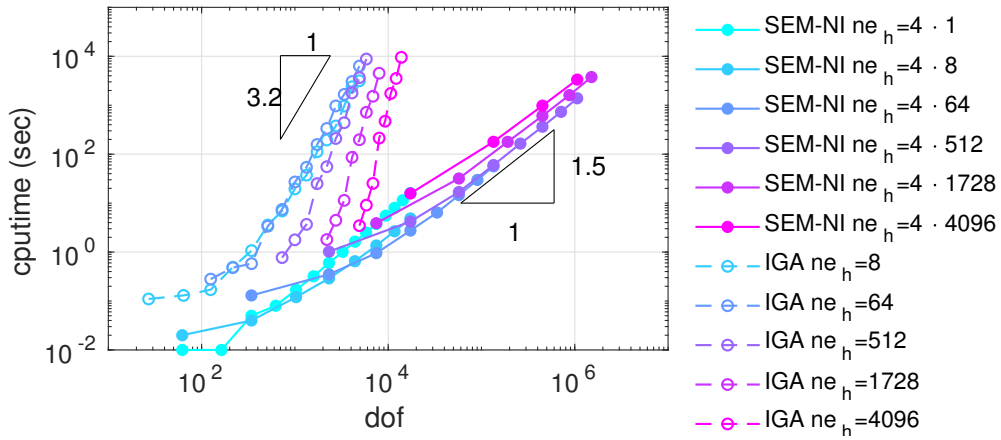

Figure 15: *One-eight of the sphere test case.* The CPUtime (in sec) needed to assemble the stiffness matrix versus the number of degrees of freedom. IGA in the legend stands for IGA-C^{p-1}

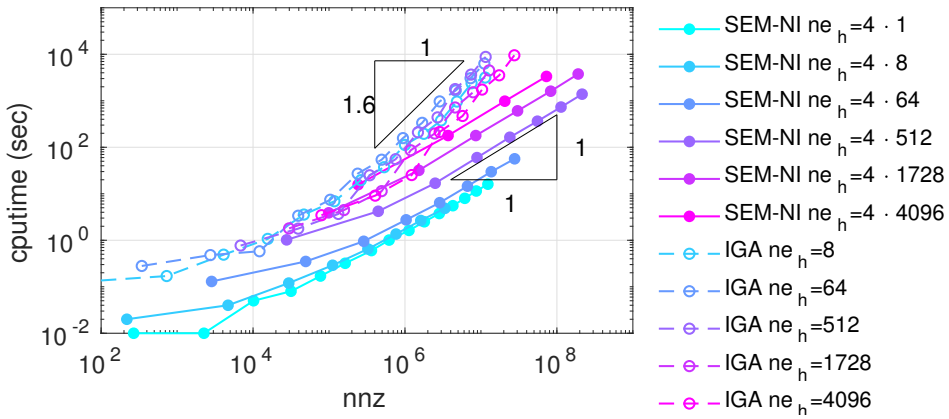

Figure 16: *One-eight of the sphere test case.* The CPUtime (in sec) needed to assemble the stiffness matrix versus the number of nonzero elements of the matrix itself. IGA in the legend stands for IGA-C^{p-1}

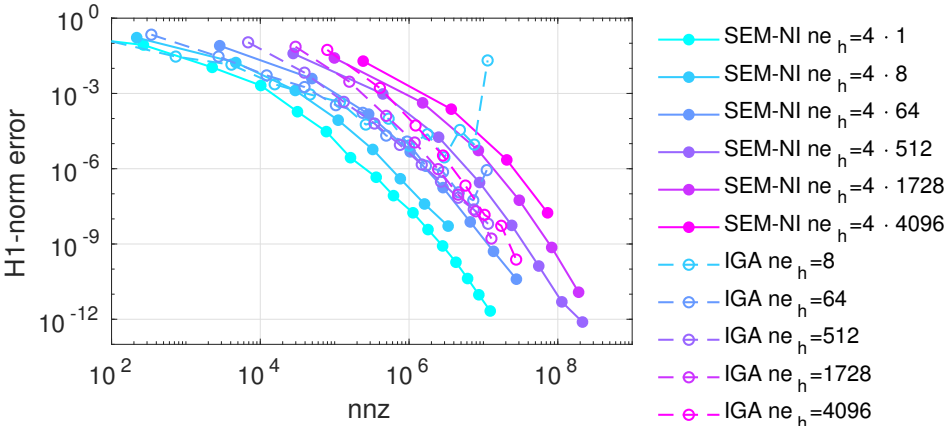

Figure 17: *One-eight of the sphere test case.* The discretization error $e_{\delta,1}$ (H^1–norm) versus the number of non-zero elements of the stiffness matrix. IGA in the legend stands for IGA-C^{p-1}

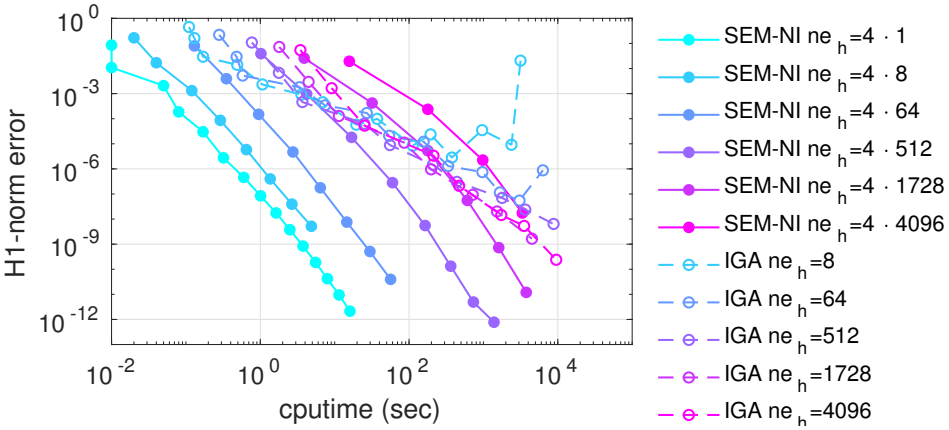

Figure 18: *One-eight of the sphere test case.* The discretization error $e_{\delta,1}$ (H^1–norm) versus the CPUtime (in sec) needed to assemble the stiffness matrix. IGA in the legend stands for IGA-C^{p-1}

4. Spectral properties: eigenvalues and condition number

In this section we summarize the main results concerning the spectral properties of SEM-NI and IGA arrays. Because of their importance for the convergence rate of iterative methods for the solution of the linear system, as well as for the propagation of rounding errors in solving the linear system itself (see, e.g., Figs. 6, 9, and 12), we specifically highlight the behavior of the extreme eigenvalues (and the corresponding spectral condition number) of mass matrices and stiffness matrices.

For any matrix A which is symmetric positive definite (or similar to a symmetric positive definite matrix), let $\lambda_{min}(A)$ and $\lambda_{max}(A)$ denote its minimum and maximum (real) eigenvalues, respectively. The *spectral condition number* of A is defined as

$$\mathcal{K}(A) = \frac{\lambda_{max}(A)}{\lambda_{min}(A)}. \tag{54}$$

The extreme eigenvalues of the SEM-NI mass matrix (14) and stiffness matrix (13) (the latter reduced to the rows and columns associated with the nodes internal to $\Omega = (0,1)^d$) behave as follows ([3, 23, 6, 7, 5]):

$$\begin{aligned}
\lambda_{min}(M_{SEM}) &\sim h^d p^{-2d} && (55)\\
\lambda_{max}(M_{SEM}) &\sim h^d p^{-d} && (56)\\
\lambda_{min}(K_{SEM}) &\sim h^d p^{-d} && (57)\\
\lambda_{max}(K_{SEM}) &\sim h^{d-2} p^{3-d} && (58)\\
\lambda_{min}((M_{SEM})^{-1} K_{SEM}) &\sim c && (59)\\
\lambda_{min}((M_{SEM})^{-1} K_{SEM}) &\sim h^{-2} p^4. && (60)
\end{aligned}$$

The corresponding iterative condition numbers for $d = 1, 2, 3$ are:

$$\begin{aligned}
\mathcal{K}(M_{SEM}) &\sim p^d && (61)\\
\mathcal{K}(K_{SEM}) &\sim p^3 h^{-2} && (62)\\
\mathcal{K}((M_{SEM})^{-1} K_{SEM}) &\sim p^4 h^{-2}; && (63)
\end{aligned}$$

these are reported in Table 3. In the whole section the symbol $\sim$ means "*up to a constant independent of both p and h*".

The eigenvalues and the condition number of IGA matrices have been studied in [15, 16]. In [15] it is proved for $d = 2$ that, independently of the k-regularity of the B-spline basis functions, it holds:

$$\begin{aligned}
&\lambda_{min}(M_k) \sim c(p)h^2, \qquad \lambda_{min}(M_k) \geq c(h)p^{-4}16^{-p}\\
&\lambda_{max}(M_k) \sim c(p)h^2, \qquad \lambda_{max}(M_k) \sim c(h)p^{-2},\\
&\mathcal{K}(M_k) \leq cp^2 16^p, \text{ with } c \text{ independent of } h \text{ and } p,\\
&\lambda_{min}(K_k) \sim c(p)h^2,\\
&\lambda_{max}(K_k) \sim c, \text{ with } c \text{ independent of } h \text{ and } p,\\
&\mathcal{K}(K_k) \leq c(h)p^8 16^p,
\end{aligned} \tag{64}$$

where M_k and K_k are the mass matrix and the stiffness matrix of IGA approximation for a generic $k = 0, \dots, p-1$. In [16] the authors prove for $d = 1$, $p \geq 1$ and $n \geq 2$ (where n is the number of elements, so that $h \sim 1/n$) that

$$\lambda_{min}(M_{p-1}) \geq c(p)h, \qquad \lambda_{min}(K_{p-1}) \geq \pi^2 c(p)h. \tag{65}$$

Other estimates about the clustering of the eigenvalues of the matrix corresponding to the IGA approximation of the advection-diffusion-reaction operator for $d = 1$ are proved in [16].

We have numerically computed the extreme eigenvalues of the mass and stiffness matrices for both IGA-C^0 and IGA-C^{p-1} using the function `eigs` of Matlab for different values of h and p. Starting from these values we have estimated the analytic behavior of the extreme eigenvalues (and then the spectral condition number) of the IGA matrices w.r.t. both h and p.

For the sake of clearness, we anticipate in Table 3 the estimated behavior of the spectral condition number of mass and stiffness matrices for all the three approaches (SEM-NI, IGA-C^0 and IGA-C^{p-1}). In the next sections we show the numerical computed values and the estimated behavior of the extreme eigenvalues and of the condition number of the mass and stiffness IGA matrices.

4.1. IGA-C^0 mass matrix

We denote with M_0 the mass matrix associated with IGA-C^0 approximation. Our numerical results show that, for any value of $h > 0$ and $p \geq 1$, $\lambda_{min}(M_0)$ and $\lambda_{max}(M_0)$ behave as:

$$\lambda_{min}(M_0) \sim h^d p^{-d/2} 4^{-pd}, \tag{66}$$
$$\lambda_{max}(M_0) \sim h^d p^{-d}, \tag{67}$$

Table 3: Behavior of the condition numbers of mass and stiffness matrices

	SEM-NI	IGA-C^0	IGA-C^{p-1}
$\mathcal{K}(M)$	$\sim p^d$	$\sim p^{-d/2} 4^{pd}$	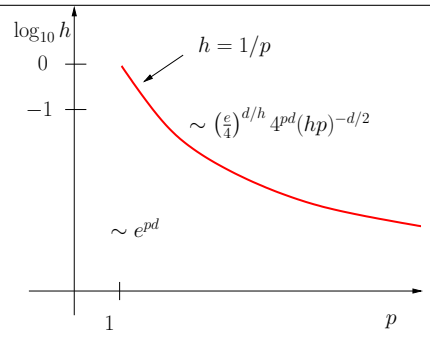
$\mathcal{K}(K)$	$\sim h^{-2} p^3$	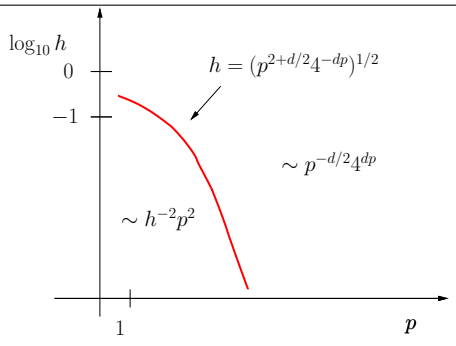	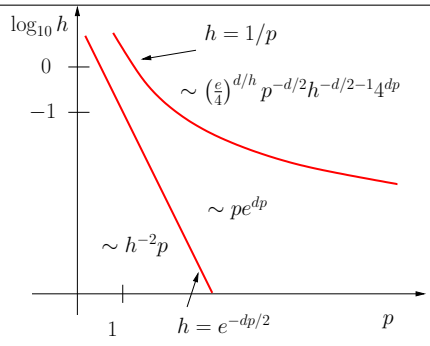

for $d = 1, 2, 3$, respectively. Then

$$\mathcal{K}(M_0) \sim p^{-d/2} 4^{pd}, \tag{68}$$

i.e., the condition number of M_0 grows exponentially with p and it is independent of the element-size h.

In Figures 19 – 21 we show the computed extreme eigenvalues and the spectral condition number versus h (at left) and versus p (at right) for $d = 1, 2, 3$. Numerical results confirm estimates (66), (67) and (68).

4.2. IGA-C^0 stiffness matrix

By denoting with K_0 the stiffness matrix corresponding to the IGA-C^0 approximation, its (computed) extreme eigenvalues behave depending as follows:

$$\lambda_{min}(K_0) \sim \begin{cases} h^d p^{-d} & \text{if } h < \left(p^{2+d/2} 4^{-dp}\right)^{1/2} \\ h^{d-2} p^{2-d/2} 4^{-dp} & \text{otherwise} \end{cases} \tag{69}$$

$$\lambda_{max}(K_0) \sim h^{d-2} p^{2-d} \tag{70}$$

for any $d = 1, 2, 3$. Then

$$\mathcal{K}(K_0) \sim \begin{cases} h^{-2} p^2 & \text{if } h < \left(p^{2+d/2} 4^{-dp}\right)^{1/2} \\ p^{-d/2} 4^{dp} & \text{otherwise.} \end{cases} \tag{71}$$

In Figure 22 we report the computed spectral condition numbers versus both h and p, for $d = 1, 2, 3$ jointly with a graph summarizing the behavior of $\mathcal{K}(K_0)$ given in (71). The stiffness matrix K_0 is better conditioned w.r.t. p when $h < (p^{2+d/2} 4^{-dp})^{1/2}$, in such a case $\mathcal{K}(K_0) \sim h^{-2} p^2$ is more favorable of one order than the condition number of K_{SEM}. On the contrary, when $h > (p^{2+d/2} 4^{-dp})^{1/2}$, $\mathcal{K}(K_0)$ grows exponentially with p, but it is independent of h.

In Figures 23 – 25 we show the computed extreme eigenvalues and the spectral condition number versus h (at left) and versus p (at right) for $d = 1, 2, 3$. Numerical results confirm estimates (66), (67) and (68).

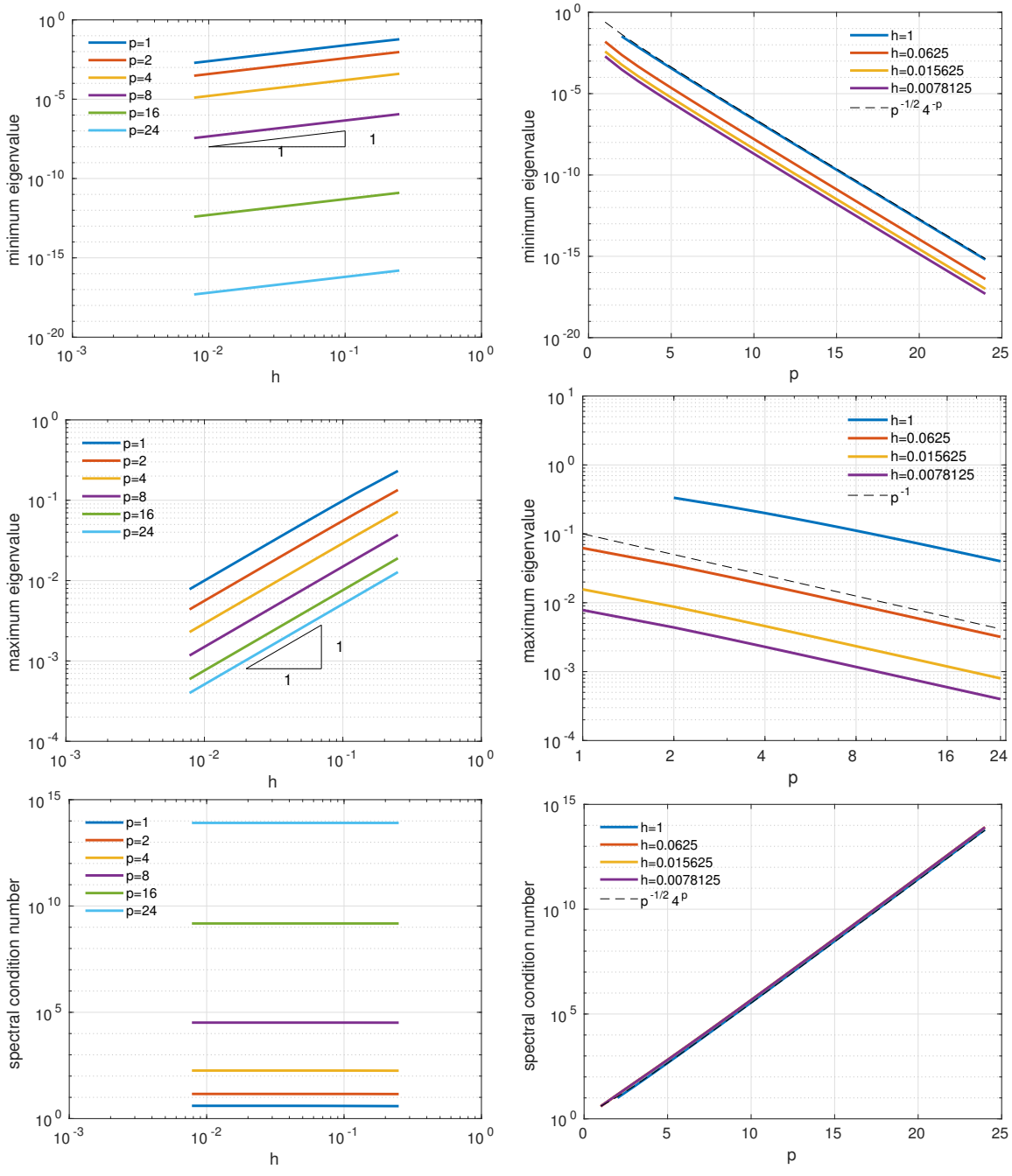

Figure 19: The extreme eigenvalues and the spectral condition number of $\mathcal{K}(M_0)$ for $d = 1$, versus h (at left) and versus p (at right). The computed values confirm the estimate given in (66), (67) and (68)

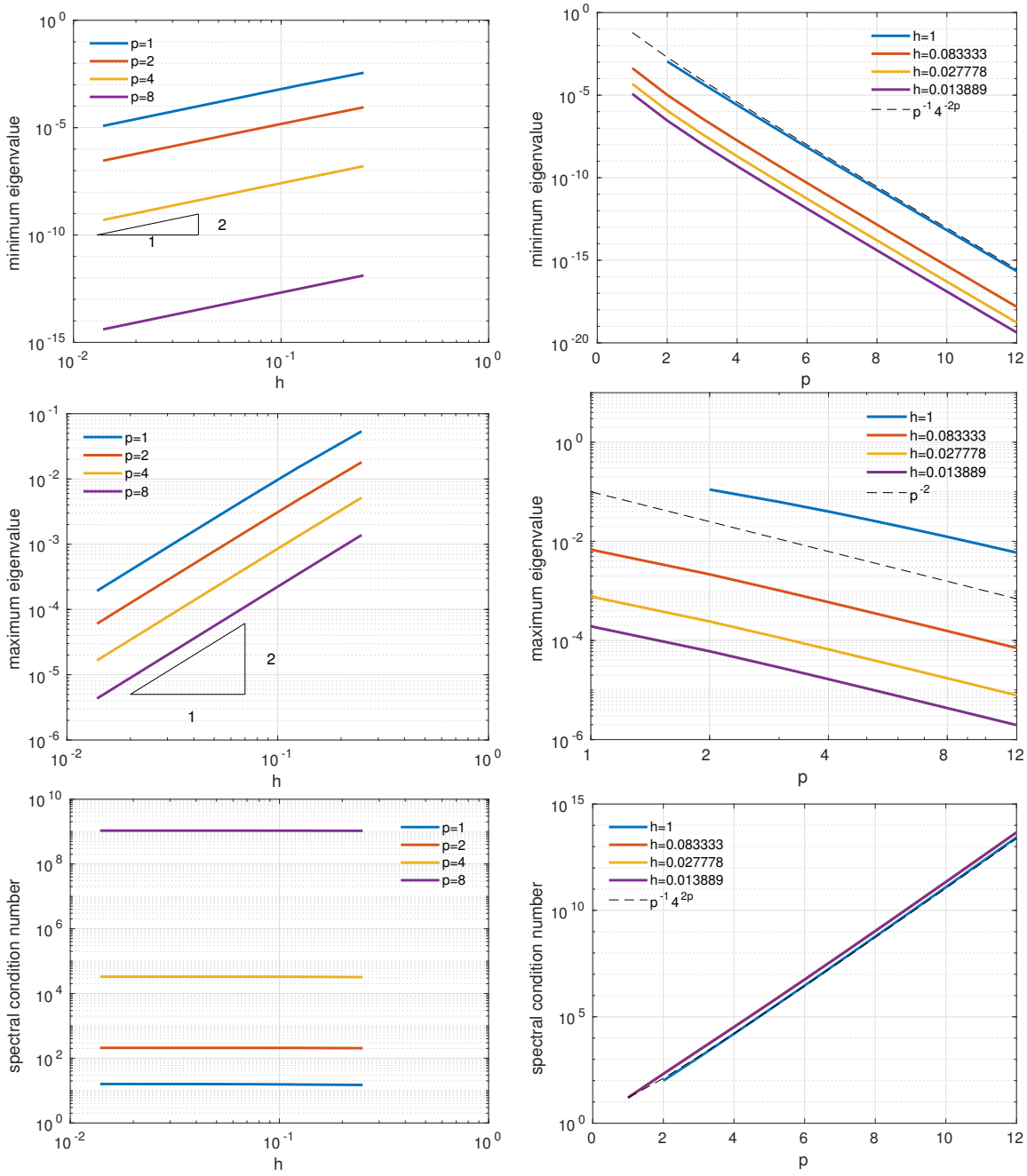

Figure 20: The extreme eigenvalues and the spectral condition number of $\mathcal{K}(M_0)$ for $d = 2$, versus h (at left) and versus p (at right). The computed values confirm the estimates given in (66), (67) and (68)

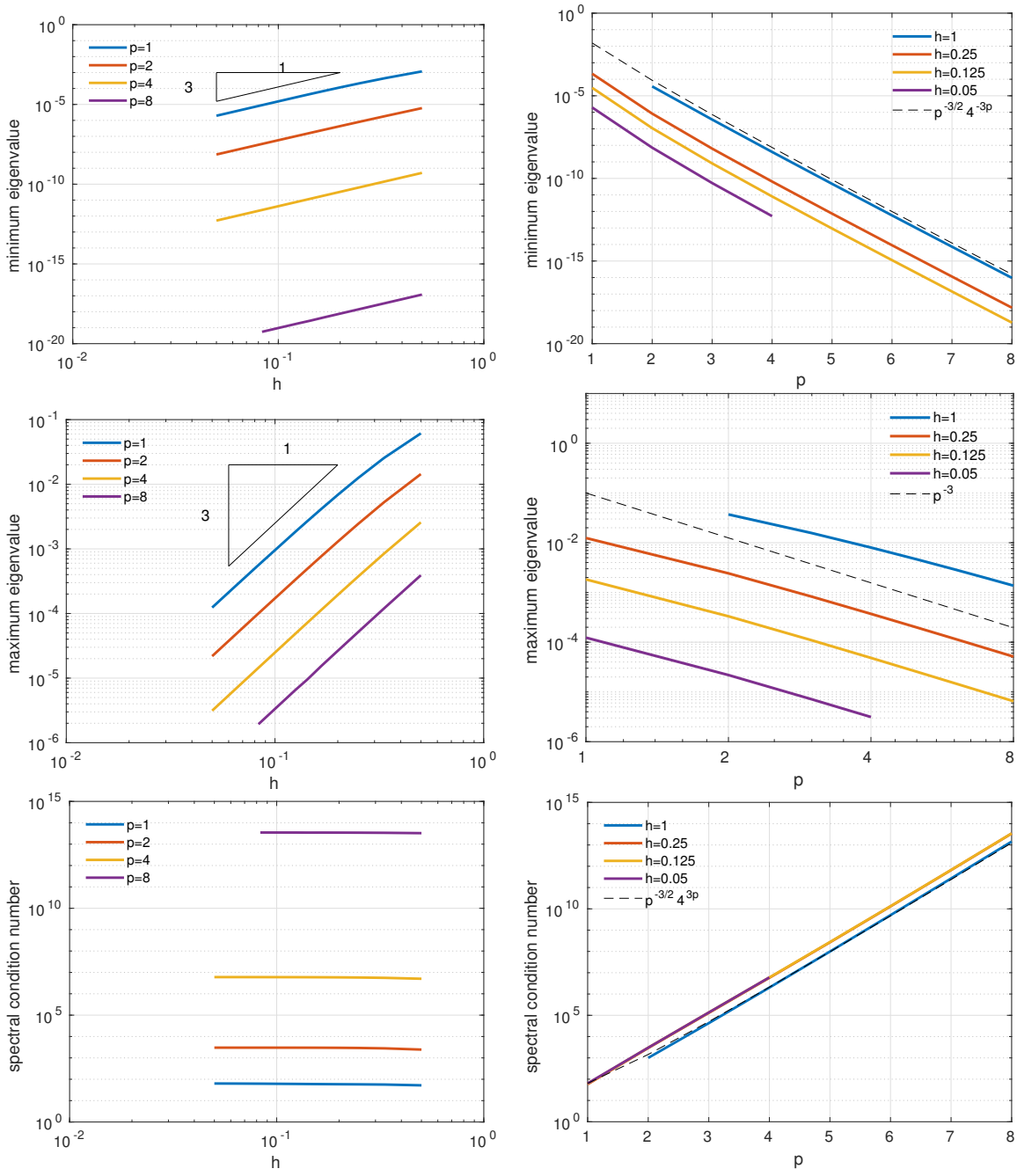

Figure 21: The extreme eigenvalues and the spectral condition number of $\mathcal{K}(M_0)$ for $d = 3$, versus h (at left) and versus p (at right). The computed values confirm the estimates given in (66), (67) and (68)

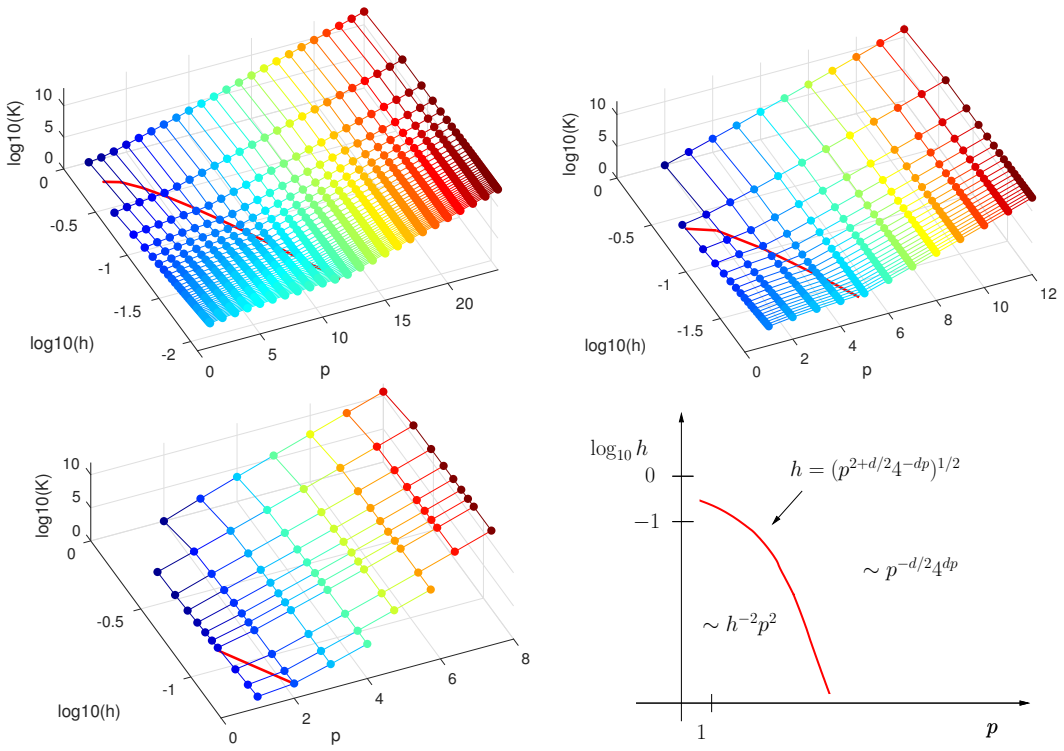

Figure 22: The numerically computed values of $\mathcal{K}(K_0)$ for $d = 1$ (top-left), $d = 2$ (top-right), and $d = 3$ (bottom-left) for different values of h and p. The red curve is the graphical representation of $h = (p^{2+d/2}4^{-dp})^{1/2}$. Summary of (71) (bottom-right)

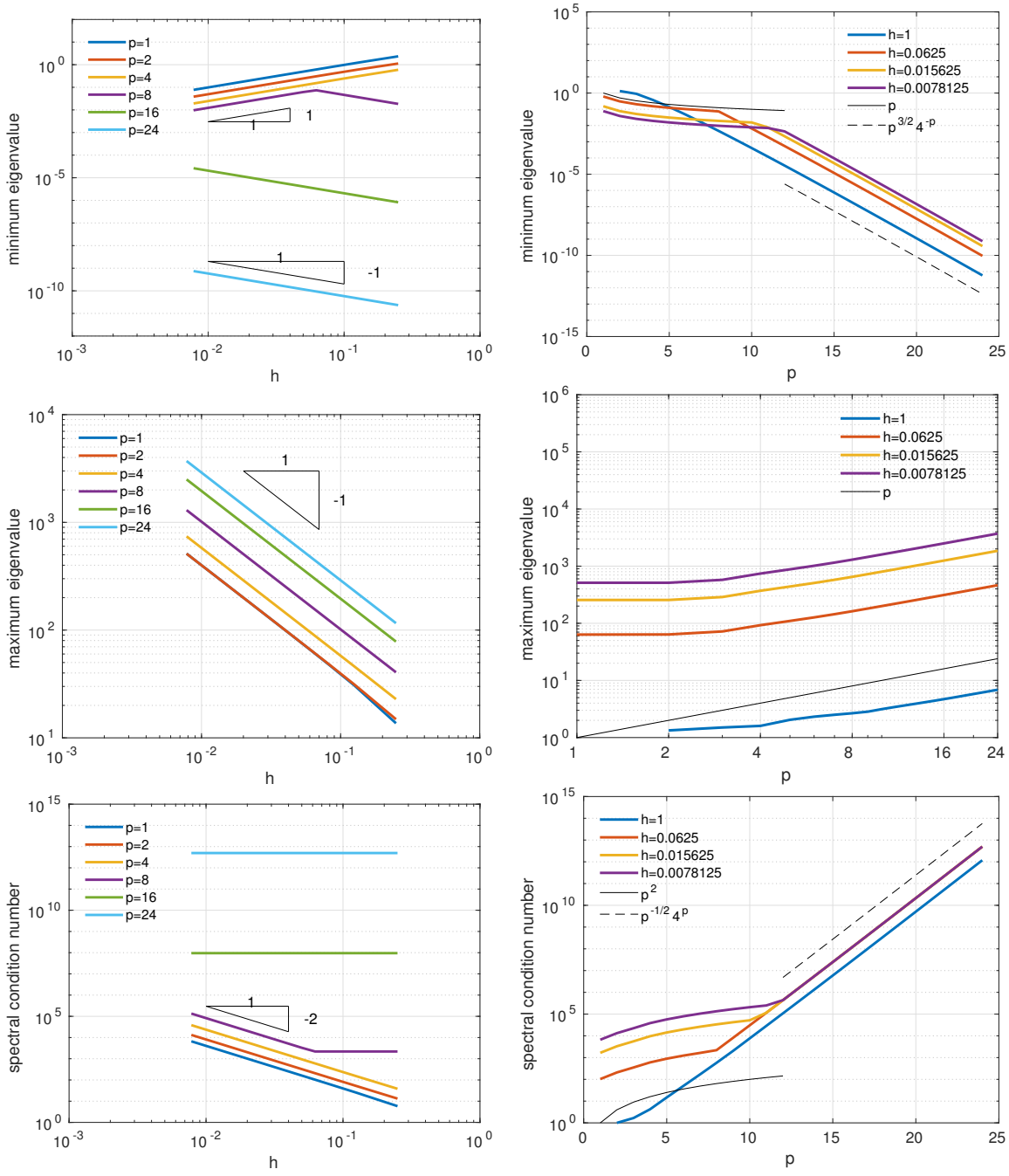

Figure 23: The extreme eigenvalues and the spectral condition number of $\mathcal{K}(K_0)$ for $d = 1$, versus h (at left) and versus p (at right). The behavior of the minimum eigenvalue (and similarly that of the spectral condition number) versus h and p depends on how much h is small w.r.t. p, see (69) and (71)

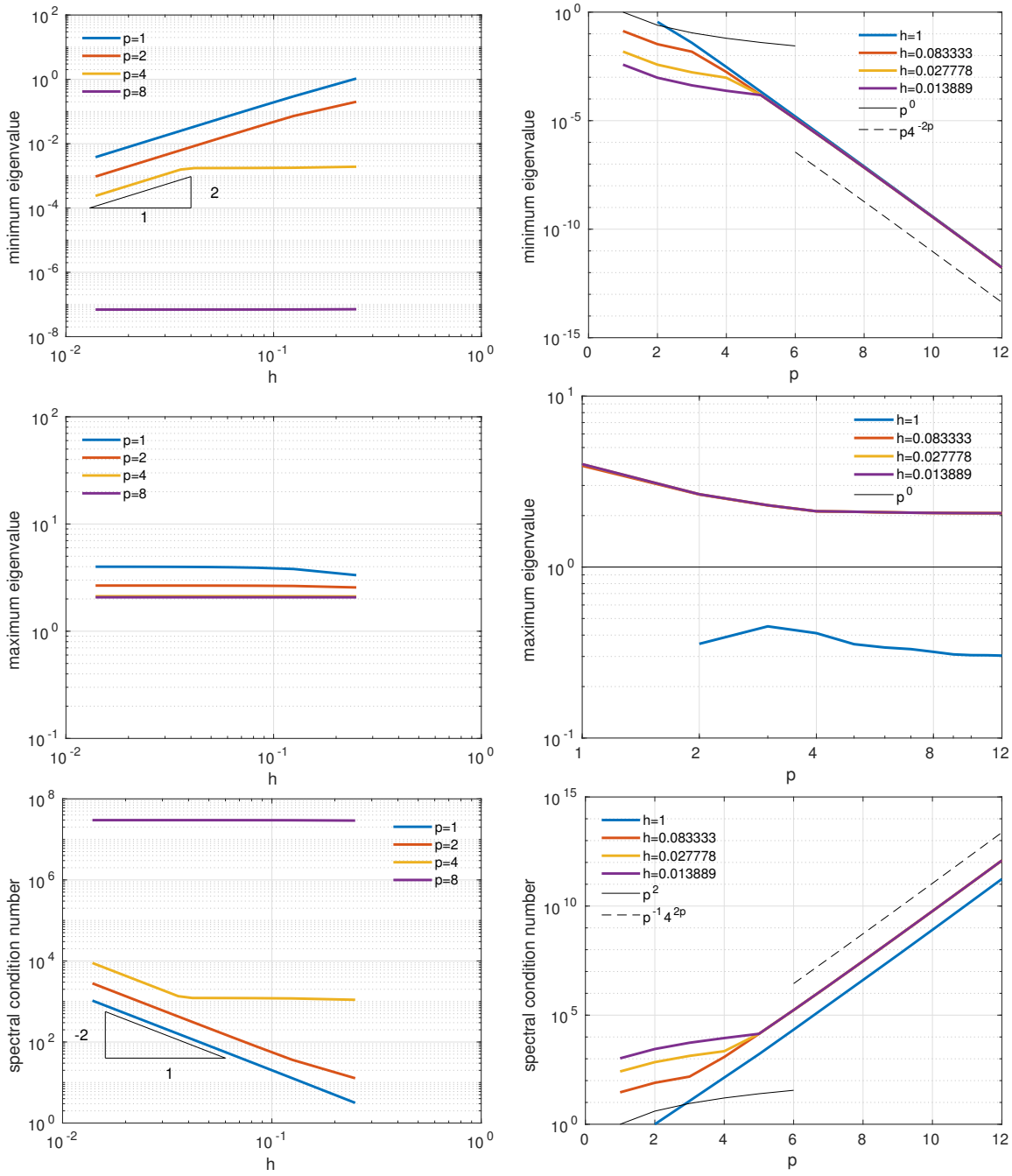

Figure 24: The extreme eigenvalues and the spectral condition number of $\mathcal{K}(K_0)$ for $d = 2$, versus h (at left) and versus p (at right). The behavior of the minimum eigenvalue (and similarly that of the spectral condition number) versus h and p depends on how much h is small w.r.t. p, see (69) and (71)

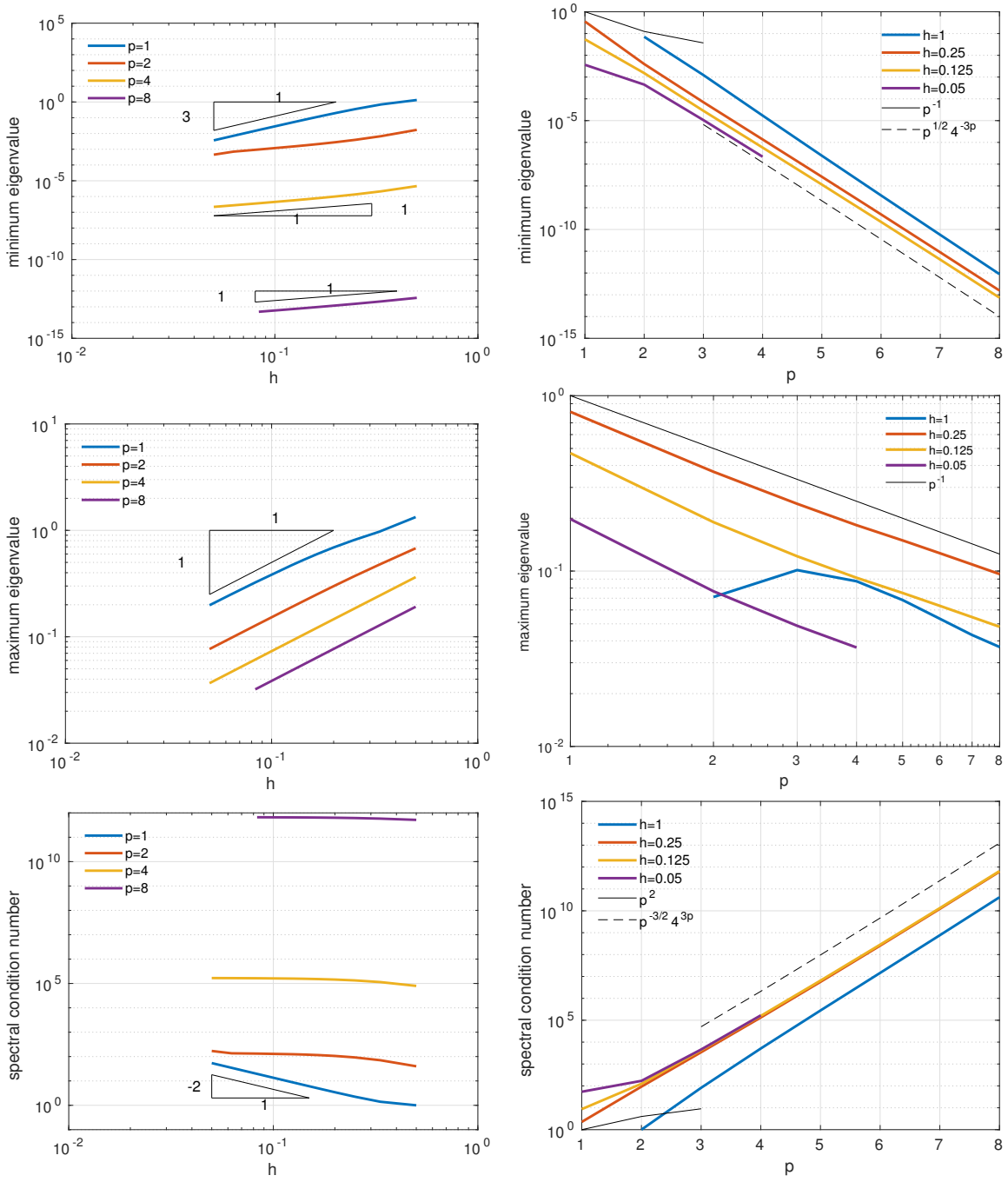

Figure 25: The extreme eigenvalues and the spectral condition number of $\mathcal{K}(K_0)$ for $d = 3$, versus h (at left) and versus p (at right). The behavior of the minimum eigenvalue (and similarly that of the spectral condition number) versus h and p depends on how much h is small w.r.t. p, see (69) and (71)

4.3. IGA-C^{p-1} mass matrix

The computed extreme eigenvalues of the mass matrix M_{p-1} of IGA-C^{p-1} behave depending on h and p as follows:

$$\lambda_{min}(M_{p-1}) \sim \begin{cases} h^d e^{-pd} & \text{if } h < 1/p \\ \left(\frac{e}{4}\right)^{-d/h} \left(\frac{h}{p}\right)^{d/2} 4^{-pd} & \text{otherwise} \end{cases} \tag{72}$$

$$\lambda_{max}(M_{p-1}) \sim \begin{cases} h^d & \text{if } h < 1/p \\ p^{-d} & \text{otherwise} \end{cases} \tag{73}$$

for any $d = 1, 2, 3$, respectively. Then

$$\mathcal{K}(M_{p-1}) \sim \begin{cases} e^{pd} & \text{if } h < 1/p \\ \left(\frac{e}{4}\right)^{d/h} (hp)^{-d/2} 4^{pd} & \text{otherwise.} \end{cases} \tag{74}$$

In Figure 26 we report the computed spectral condition numbers versus both h and p, for $d = 1, 2, 3$ jointly with a graph summarizing the behavior of $\mathcal{K}(M_{p-1})$ given in (74).

In Figures 27 – 29 we show the computed extreme eigenvalues and the spectral condition number versus h (at left) and versus p (at right) for $d = 1, 2, 3$. Numerical results confirm estimates (72), (73) and (74).

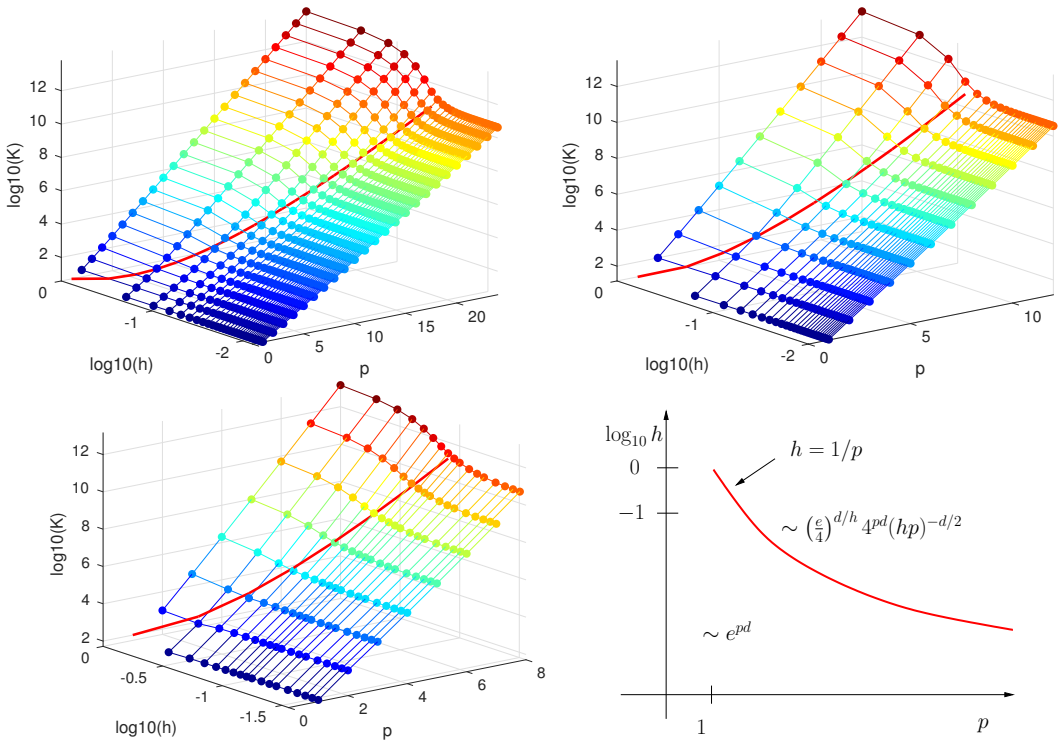

Figure 26: The numerically computed values of $\mathcal{K}(M_{p-1})$ for $d = 1$ (top-left), $d = 2$ (top-right), and $d = 3$ (bottom-left) for different values of h and p. The red curve is the graphical representation of $h = 1/p$. Summary of (74) (bottom-right)

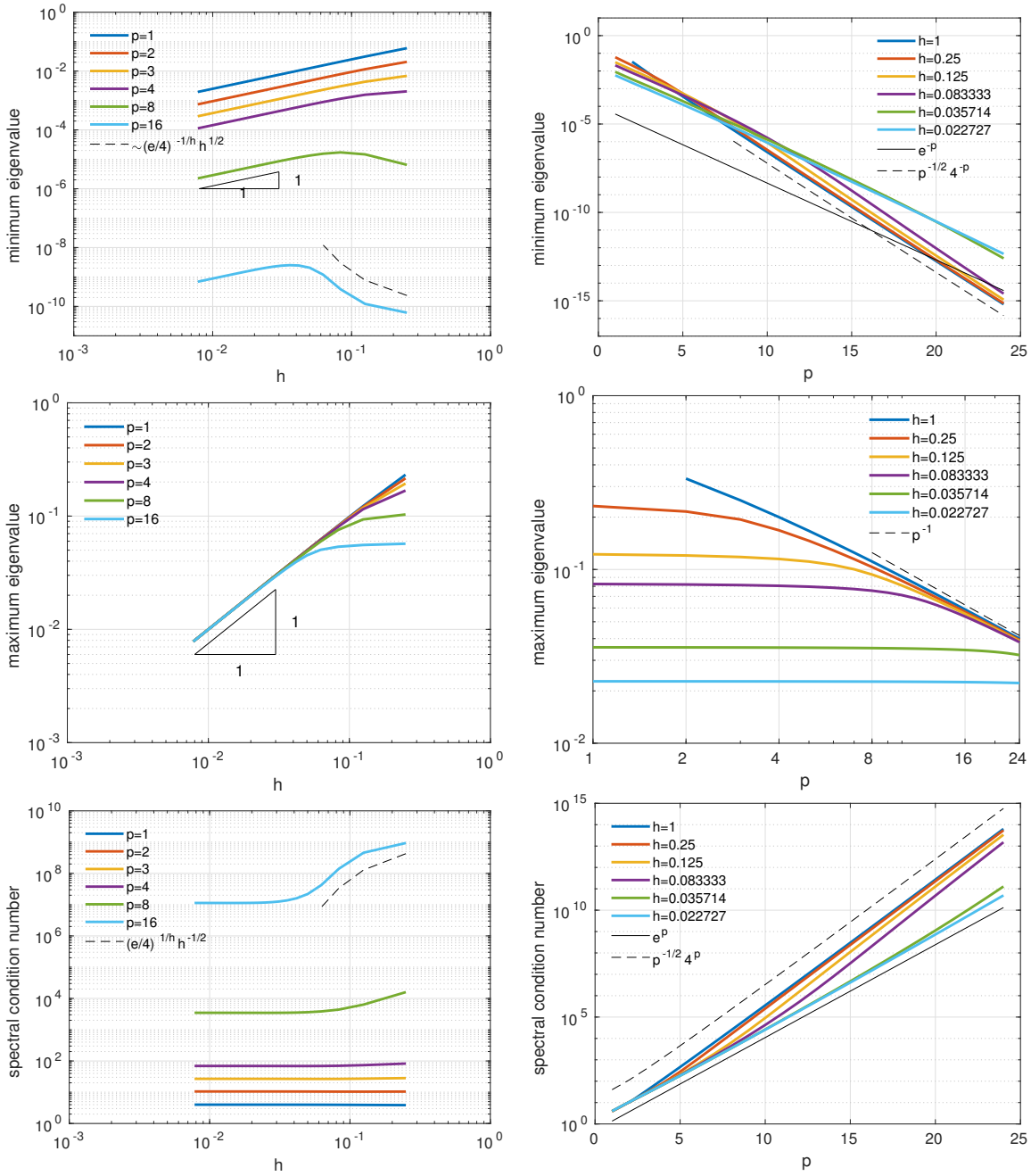

Figure 27: The extreme eigenvalues and the spectral condition number of $\mathcal{K}(M_{p-1})$ for $d = 1$, versus h (at left) and versus p (at right). The behavior of the extreme eigenvalues (and similarly that of the spectral condition number) versus h and p depends on how much h is small w.r.t. p, see (72)–(74)

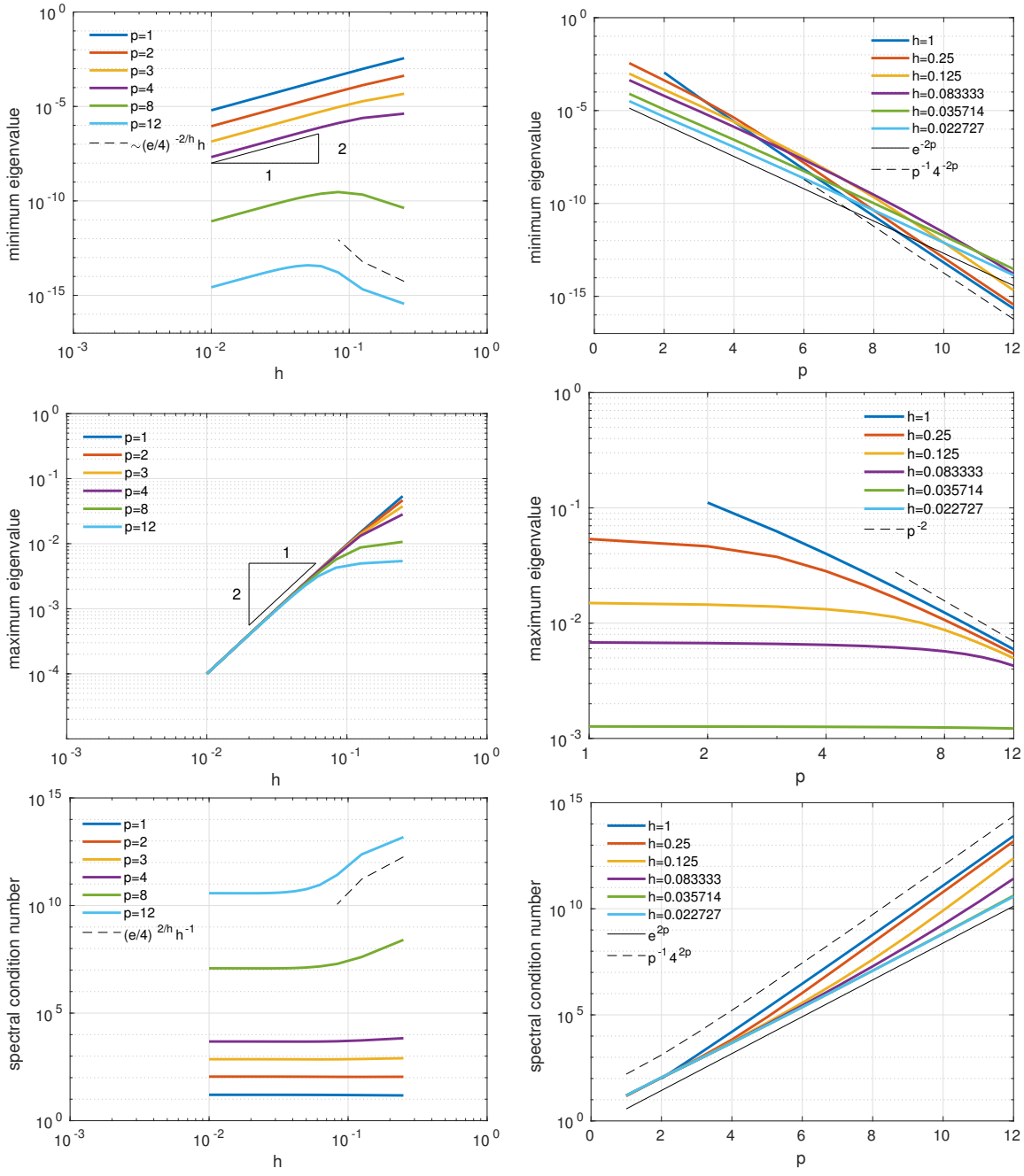

Figure 28: The extreme eigenvalues and the spectral condition number of $\mathcal{K}(M_{p-1})$ for $d = 2$, versus h (at left) and versus p (at right). The behavior of the extreme eigenvalues (and similarly that of the spectral condition number) versus h and p depends on how much h is small w.r.t. p, see (72)–(74)

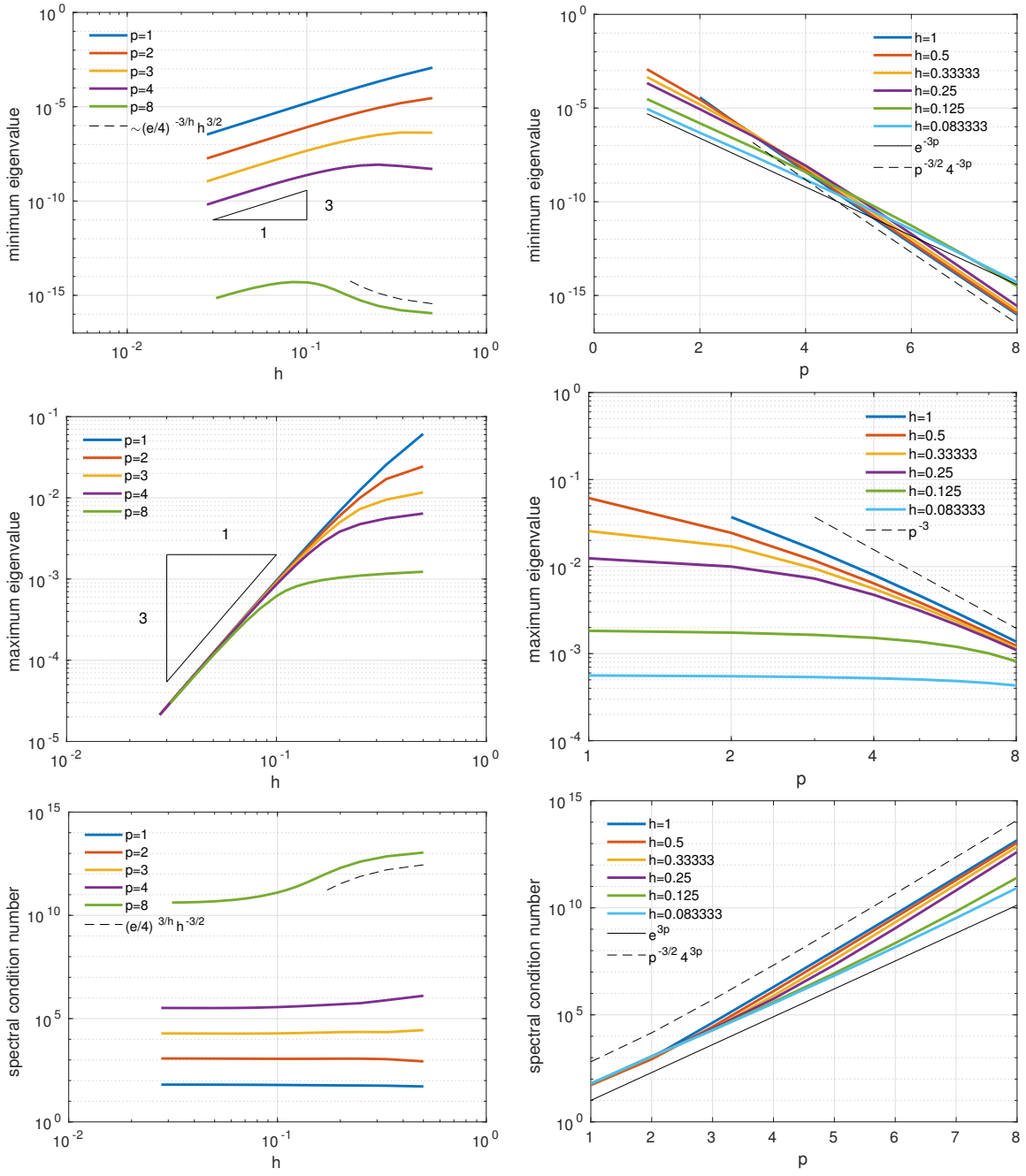

Figure 29: The extreme eigenvalues and the spectral condition number of $\mathcal{K}(M_{p-1})$ for $d = 3$, versus h (at left) and versus p (at right). The behavior of the extreme eigenvalues (and similarly that of the spectral condition number) versus h and p depends on how much h is small w.r.t. p, see (72)–(74)

4.4. IGA-C^{p-1} stiffness matrix

The computed extreme eigenvalues of the stiffness matrix K_{p-1} of IGA-C^{p-1} behave depending on h and p as follows:

$$\lambda_{min}(K_{p-1}) \sim \begin{cases} h^d & \text{if } h < e^{-pd/2} \\ h^{d-2}e^{-pd} & \text{if } e^{-pd/2} < h < 1/p \\ \left(\frac{e}{4}\right)^{-d/h} p^{2-d/2} h^{d/2} 4^{-pd} & \text{if } h > 1/p \end{cases} \tag{75}$$

$$\lambda_{max}(K_{p-1}) \sim \begin{cases} ph^{d-2} & \text{if } h < 1/p \\ p^{2-d}h^{-1} & \text{otherwise.} \end{cases} \quad \text{for } p > 2 \tag{76}$$

for any $d = 1, 2, 3$, respectively. Then

$$\mathcal{K}(K_{p-1}) \sim \begin{cases} h^{-2}p & \text{if } h < e^{-dp/2} \\ pe^{dp} & \text{if } e^{-dp/2} < h < 1/p \\ \left(\frac{e}{4}\right)^{d/h} p^{-d/2} h^{-d/2-1} 4^{dp} & \text{otherwise} \end{cases} \tag{77}$$

In Figure 30 we report the computed spectral condition numbers versus both h and p, for $d = 1, 2, 3$ jointly with a graph summarizing the behavior of $\mathcal{K}(K_{p-1})$ given in (77).

In Figures 31 – 33 we show the computed extreme eigenvalues and the spectral condition number versus h (at left) and versus p (at right) for $d = 1, 2, 3$. Numerical results confirm estimates (75), (76) and (77).

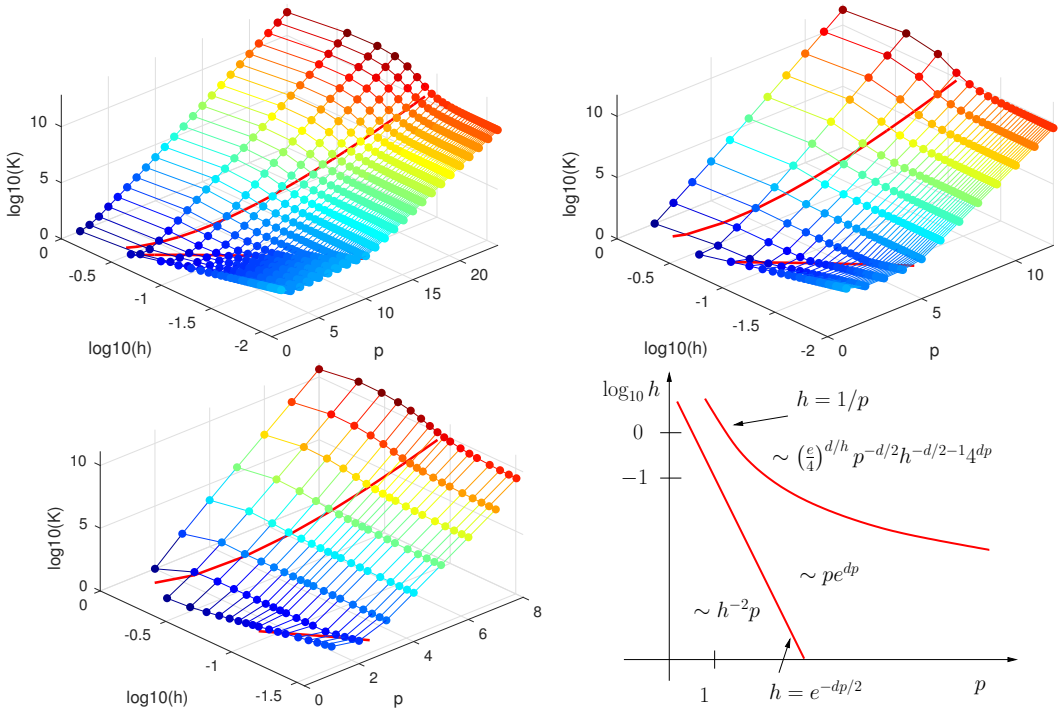

Figure 30: The numerically computed values of $\mathcal{K}(K_{p-1})$ for $d = 1$ (top-left), $d = 2$ (top-right), and $d = 3$ (bottom-left) for different values of h and p. The red curves are the graphical representations of $h = e^{-dp/2}$ and $h = 1/p$. Summary of (77) (bottom-right)

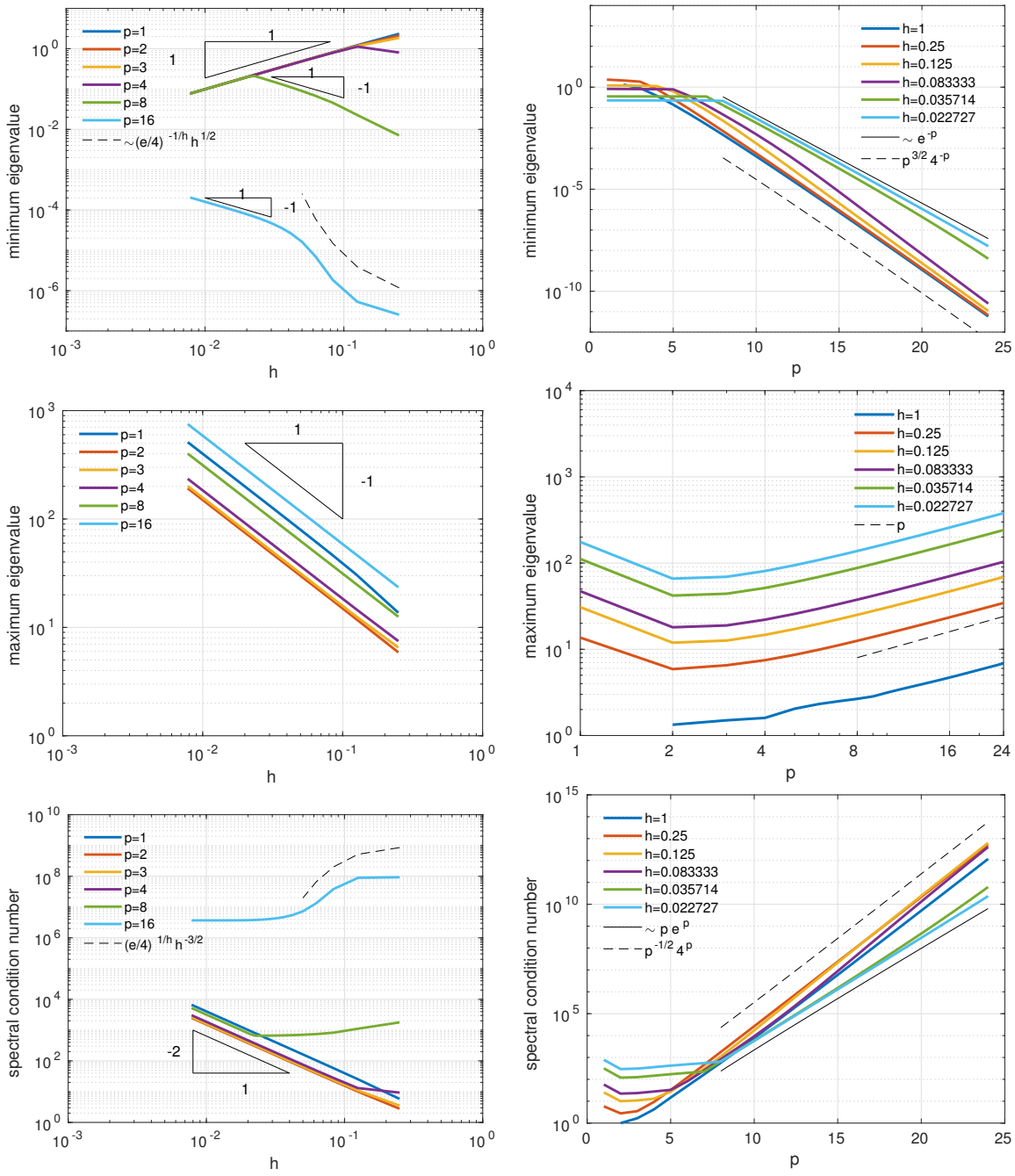

Figure 31: The extreme eigenvalues and the spectral condition number of $\mathcal{K}(K_{p-1})$ for $d = 1$, versus h (at left) and versus p (at right). The behavior of the extreme eigenvalues (and similarly that of the spectral condition number) versus h and p depends on how much h is small w.r.t. p, see (75)–(77)

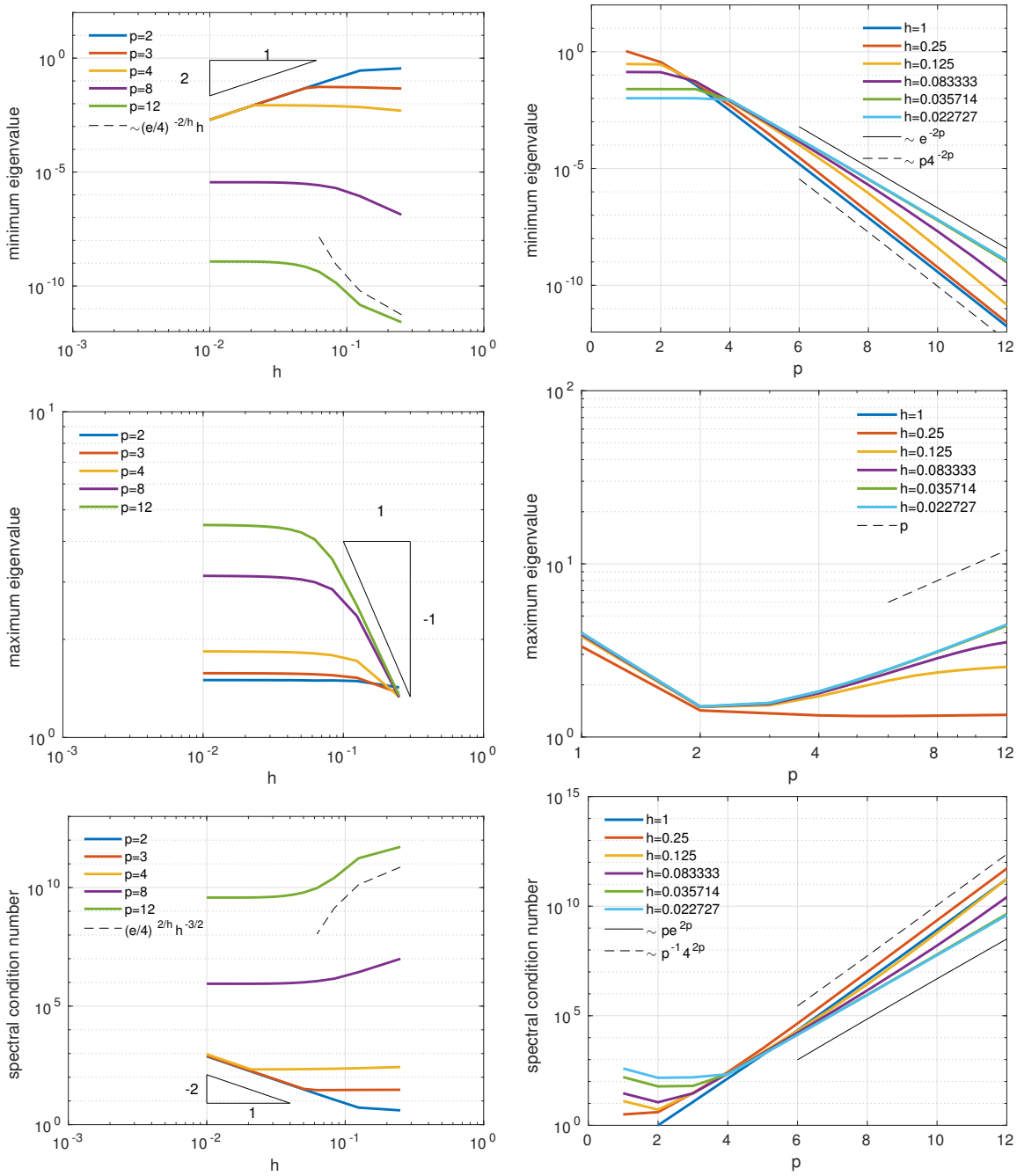

Figure 32: The extreme eigenvalues and the spectral condition number of $\mathcal{K}(K_{p-1})$ for $d = 2$, versus h (at left) and versus p (at right). The behavior of the extreme eigenvalues (and similarly that of the spectral condition number) versus h and p depends on how much h is small w.r.t. p, see (75)–(77)

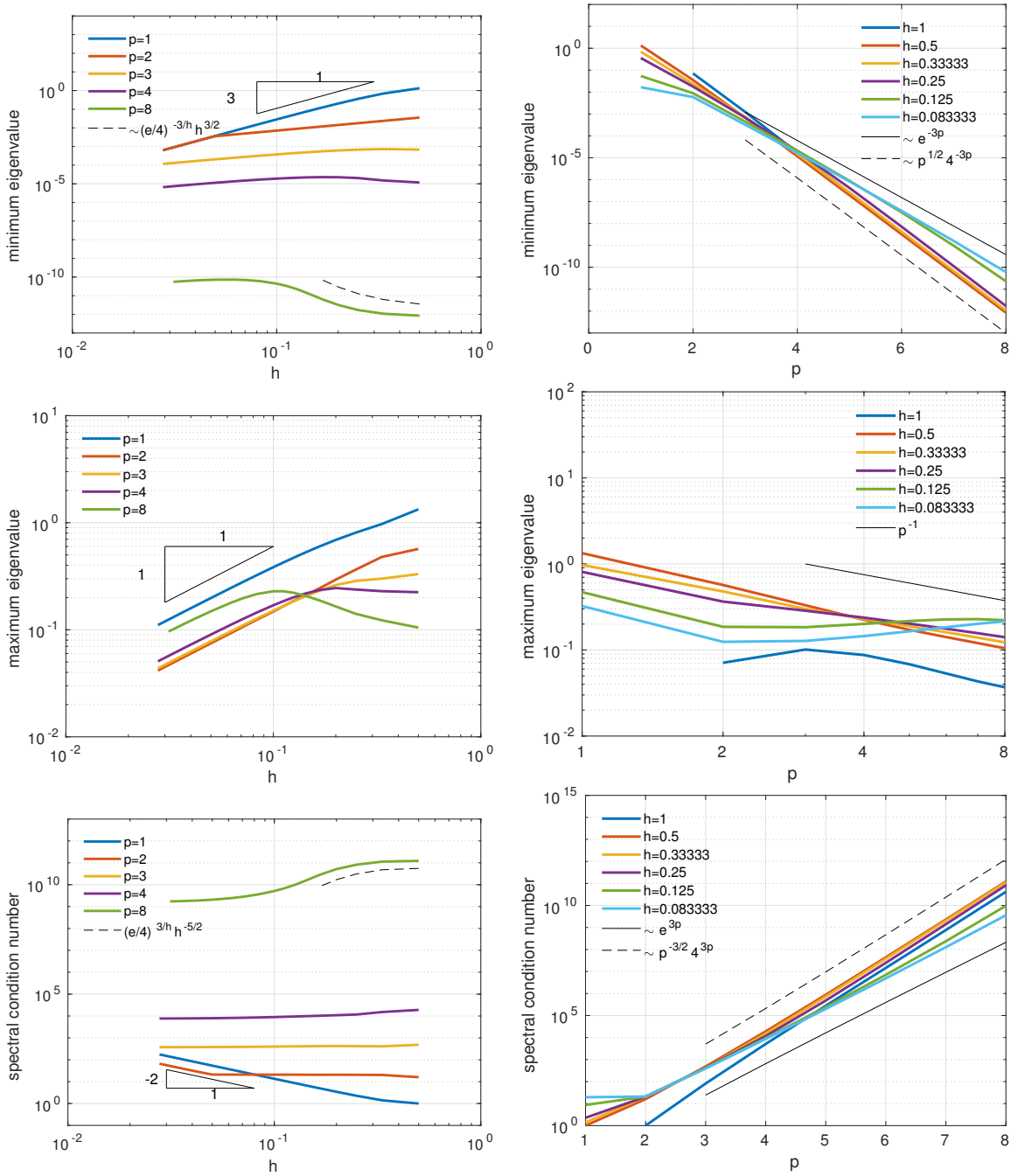

Figure 33: The extreme eigenvalues and the spectral condition number of $\mathcal{K}(K_{p-1})$ for $d = 3$, versus h (at left) and versus p (at right). The behavior of the extreme eigenvalues (and similarly that of the spectral condition number) versus h and p depends on how much h is small w.r.t. p, see (75)–(77)

5. Conclusions

In this paper we have carried out a systematic comparison between the Spectral Element Method with Numerical Integration (SEM-NI) and the NURBS-based Isogeometric Analysis methods (in the framework of the Galerkin method) IGA-C^0 (C^0 regularity inside the domain) and IGA-C^{p-1} (global C^{p-1} regularity inside the domain). Our focus has been on the accuracy and the conditioning with respect to the discretization parameters h and p when applied to solve the Poisson problem. As of accuracy, we have considered two test cases, the first one on the reference domain $\Omega = (0,1)^d$ with $d = 1, 2, 3$, the second one on a more general domain with curved boundary. IGA and SEM-NI are comparable in terms of accuracy w.r.t. h and p, whereas their computational costs are different. As a matter of fact, for a given accuracy target, SEM-NI is the less computational demanding method both in terms of CPUtime and of memory storage.

In the second part of the paper, starting from the numerical computations of the eigenvalues, we provided very accurate estimates of the extreme eigenvalues (as well as of the spectral condition numbers) of the mass and stiffness matrices of IGA approaches. These factors play a crucial role on the convergence rate of iterative methods for the solution of the associated linear system and on the propagation of rounding errors in solving the linear system itself. The extreme eigenvalues also reflect the stability restriction of explicit time-advancing schemes for initial boundary value problems. The condition number of IGA mass matrices grows exponentially w.r.t. to p, while the condition number of the SEM-NI matrices grows only algebraically vs p. On the other hand, the condition number of the IGA stiffness matrices follows different regimes (with either algebraic or exponential dependence on p) in different regions of the plane (p, h).

References

[1] A. Bartezzaghi, L. Dedè, and A. Quarteroni. Isogeometric Analysis for high order Partial Differential Equations on surfaces. *Comp. Methods Appl. Mech. Engrg*, 295:446–469, 2015.

[2] Y. Bazilevs, L. Beirão da Veiga, J.A. Cottrell, T.J.R. Hughes, and G. Sangalli. Isogeometric analysis: Approximation, stability and error estimates for h-refined meshes. *Math. Models Methods Appl. Sci.*, 16:1–60, 2006.

[3] C. Bernardi and Y. Maday. *Approximations Spectrales de Problèmes aux Limites Elliptiques*. Springer Verlag, Paris, 1992.

[4] C. Bernardi and Y. Maday. Spectral methods. In *Handbook of numerical analysis, Vol. V*, Handb. Numer. Anal., V, pages 209–485. North-Holland, Amsterdam, 1997.

[5] C. Canuto, P. Gervasio, and A. Quarteroni. Finite-Element Preconditioning of G-NI Spectral Methods. *SIAM J. Sci. Comput.*, 31(6):4422–4451, 2009/10.

[6] C. Canuto, M. Y. Hussaini, A. Quarteroni, and T. A. Zang. *Spectral Methods. Fundamentals in Single Domains*. Springer, Heidelberg, 2006.

[7] C. Canuto, M. Y. Hussaini, A. Quarteroni, and T. A. Zang. *Spectral Methods. Evolution to Complex Geometries and Applications to Fluid Dynamics*. Springer, Heidelberg, 2007.

[8] J.A. Cottrell, T.J.R. Hughes, and Y. Bazilevs. *Isogeometric Analysis: Toward Integration of CAD and FEA*. Wiley, 2009.

[9] J.A. Cottrell, T.J.R. Hughes, and A. Reali. Studies of refinement and continuity in Isogeometric structural analysis. *Comput. Methods Appl. Mech. Engrg.*, 196:4160–4183, 2007.

[10] L. Beirão da Veiga, A. Buffa, J. Rivas, and G. Sangalli. Some estimates for *h-p-k*-refinement in isogeometric analysis. *Numer. Math.*, 118(2):271–305, 2011.

[11] L. Beirão da Veiga, A. Buffa, G. Sangalli, and R. Vàzquez. An introduction to the numerical analysis of isogeometric methods. In *Numerical simulation in physics and engineering*, volume 9 of *SEMA SIMAI Springer Ser.*, pages 3–69. Springer, 2016.

[12] L. Dedè and A. Quarteroni. Isogeometric Analysis for second order partial differential equations on surfaces. *Comp. Methods Appl. Mech. Engrg.*, 284:807–834, 2015.

[13] L. Dedè and H.A.F.A. Santos. B-spline goal–oriented error estimators for geometrically nonlinear rods. *Comp. Mech.*, 49(1):35–52, 2012.
[14] J.A. Evans, Y. Bazilevs, I. Babuška, and T.J.R. Hughes. n–widths, sup–infs, and optimality ratios for the k–version of the Isogeometric finite element method. *Comput. Methods Appl. Mech. Engrg.*, 198:1726–1741, 2009.
[15] K. Gahalaut and S. Tomar. Condition number estimates for matrices arising in the isogeometric discretizations. Technical Report 2012-23, RICAM, 2012.
[16] C. Garoni, C. Manni, F. Pelosi, S. Serra Capizzano, and H. Speleers. On the spectrum of stiffness matrices arising from isogeometric analysis. *Numer. Math.*, 127(4):751–799, 2014.
[17] W.J. Gordon and C.A. Hall. Construction of curvilinear co-ordinate systems and their application to mesh generation. *Int. J. Numer. Meth. Eng.*, 7:461–477, 1973.
[18] W.J. Gordon and C.A. Hall. Transfinite element methods: blending-function interpolation over arbitrary curved element domains. *Numer. Math.*, 21:109–129, 1973.
[19] W.J. Gordon and L.C. Thiel. Transfinite mappings and their application to grid generation. *App. Math. Comput.*, 10:171–233, 1982.
[20] J. Kiendl, F. Auricchio, T.J.R. Hughes, and A. Reali. Single-variable formulations and isogeometric discretizations for shear deformable beams. *Comp. Methods Appl. Mech. Engrg.*, 284:988–1004, 2015.
[21] J. Kiendl, M.C. Hsu, M.C.H. Wu, and A. Reali. Isogeometric Kirchhoff–Love shell formulations for general hyperelastic materials. *Comp. Methods Appl. Mech. Engrg.*, 291:280–303, 2015.
[22] F. Maurin, L. Dedè, and A. Spadoni. Isogeometric rotation–free analysis of planar extensible–elastica for static and dynamic applications. *Nonlinear Dyn.*, 81(1–2):77–96, 2015.
[23] J.M. Melenk. On condition numbers in *hp*-FEM with Gauss-Lobatto-based shape functions. *J. Comput. Appl. Math.*, 139(1):21–48, 2002.
[24] A. Quarteroni and A. Valli. *Numerical Approximation of Partial Differential Equations*. Springer Verlag, Heidelberg, 1994.
[25] A. Tagliabue, L. Dedè, and A. Quarteroni. Isogeometric analysis and error estimates for high order partial differential equations in fluid dynamics. *Comput. Fluids*, 102:277–303, 2014.
[26] H.A. van der Vorst. *Iterative Krylov methods for large linear systems*. Cambridge University Press, Cambridge, 2003.
[27] R. Vàzquez. A new design for the implementation of isogeometric analysis in octave and matlab: Geopdes 3.0. *Comput. Math. Appl.*, 72(3):523–554, 2016.

MOX Technical Reports, last issues

Dipartimento di Matematica
Politecnico di Milano, Via Bonardi 9 - 20133 Milano (Italy)

20/2018 Bassi, C. ; Abbà, A.; Bonaventura L.; Valdettaro, L.
A priori tests of a novel LES approach to compressible variable density turbulence

19/2018 Menghini, F.; Dede', L.; Quarteroni, A.
Variational Multiscale LES modeling of blood flow in an idealized left human heart

18/2018 Antonietti, P.F.; Bonaldi, F.; Mazzieri, I.
A high-order discontinuous Galerkin approach to the elasto-acoustic problem

17/2018 Agosti, A.; Giverso, C.; Faggiano, E.;Stamm,A.; Ciarletta, P.
A personalized mathematical tool for neuro-oncology: a clinical case study

16/2018 Calissano, A.; Vantini, S.; Arnaboldi, M.
An elephant in the room: Twitter samplingmethodology.

15/2018 Simona, A.; Bonaventura, L.; Pugnat, T.; Dalena, B.
High order time integrators for the simulation of charged particle motion in magnetic quadrupoles

14/2018 Cuffaro, M.; Miglio, E.; Penati, M.;Viganò, M.
Mantle upwelling driven by asymmetric sea-floor spreading at northern Mid–Atlantic ridge

13/2018 Gandelli, E.; Penati, M.;Quaglini, V.;Lomiento, G.; Miglio, E.; Benzoni, G.M.
A novel OpenSees element for single curved surface sliding isolators

11/2018 Delpopolo Carciopolo L.; Bonaventura L.; Scotti A.; Formaggia L.
A conservative implicit multirate method for hyperbolic problems

12/2018 Dal Santo, N.; Deparis, S.; Manzoni, A.; Quarteroni, A.
Multi space reduced basis preconditioners for large-scale parametrized PDEs